

Magnetic dual chiral density wave phase in rotating cold quark matter

H. Mortazavi Ghalati* and N. Sadooghi[†]

Department of Physics, Sharif University of Technology, P.O. Box 11155-9161, Tehran, Iran

The effect of rotation on the formation of the magnetic dual chiral density wave (MDCDW) in a dense and magnetized cold quark matter is studied. This phase is supposed to exist in the extreme conditions prevailing, e.g., in a neutron star. These conditions are, apart from high densities and strong magnetic fields, a relatively large angular velocity. To answer the question of whether the rotation enhances or suppresses the formation of this phase, we first determine the effect of rotation on the energy dispersion relation of a fermionic system in the presence of a constant magnetic field and then focus on the thermodynamic potential of the model at low temperature T and finite chemical potential μ . The thermodynamic potential consists, in particular, of an anomalous part leading to certain topological effects. We show that in comparison with the nonrotating case, a term proportional to the angular velocity appears in this anomalous potential. We then solve the corresponding gap equations to the chiral and spatial modulation condensates, and study the dependence of these dynamical variables on the chemical potential (μ), magnetic field (eB), and angular velocity (Ω). It turns out that the interplay between these parameters suppresses the formation of the MDCDW phase in relevant regimes for cold neutron stars. This is interpreted as the manifestation of the inverse magnetorotational catalysis, which is also reflected in the phase portraits $eB-\mu$, $eB-\Omega R$, and $\mu-\Omega R$, explored in this work.

I. INTRODUCTION

Exploring the phase diagram of quark matter under extreme conditions is one of the important subjects in nuclear physics. These conditions are, among others, high temperature, large baryon chemical potential, and the presence of uniform electromagnetic fields. Big questions related to these subjects are discussed in [1]. Open problems and possible past, present, and future theoretical and experimental strategies to answer these questions are discussed recently in various reports and reviews [2–5]. Apart from standard simulation methods in lattice Quantum Chromodynamics (QCD) [3], new computational tools, such as machine learning [6], are developed and applied to either analyze the experimental data or to overcome the deficiencies of standard methods in working with QCD under extreme conditions.

Neutron stars are the natural playground to study quark matter under extreme conditions. These stars, which are produced by gravitational collapse of very massive stars, are the densest objects in the Universe. Their inner density is several times larger than the nuclear saturation mass density $\rho_n \sim 2.5 \times 10^{17} \text{ kg/m}^3$ (see e.g. [7]). There have been several attempts to determine the equation of states of neutron stars [8]. The latter is a necessary input for the Tolman–Oppenheimer–Volkoff equation, which together with the mass continuity equation yields the mass-to-radius ratio of these stars [9]. Using effective models, like the Nambu–Jona-Lasinio (NJL) model, it was found that the matter in the interior of neutron stars is in the color superconductivity (CS) phase [10]. In particular, the three-flavor color-flavor locked (CFL) phase seemed to be the most favored phase [11].

The CFL phase, however, does not pass certain astrophysical tests [12], and is thus ruled out.

Apart from large densities, neutron stars exhibit very strong magnetic fields. The strength of the magnetic fields of magnetars is estimated to be $\sim 10^{18} \text{ G}$ for nuclear matter and $\sim 10^{20} \text{ G}$ for quark matter (see [12] and references therein). The effect of constant magnetic fields on CS phases is studied, e.g. in [13]. In [14], it is shown that the two-flavor CS phase is also favorable in a magnetized quark matter at intermediate chemical potentials. By increasing the baryon density from low values to densities a few times higher than the nuclear saturation density, another phase can be formed at low temperatures. This phase, originally introduced in [15] and studied in several follow-up papers, e.g. [16], is characterized by quark-hole pairs having a finite total momentum and leading to standing waves. In [17], in analogy to the static spin density waves, known from condensed matter physics, a density wave is introduced in quark matter at moderate densities which is referred to as the “dual chiral density wave”. It is represented by a dual standing wave in scalar and pseudoscalar condensates. The effect of uniform magnetic fields on the formation of this phase is studied for the first time in [18]. The corresponding phase is dubbed the MDCDW phase. It is characterized by two dynamical variables, chiral and spatial modulation condensates, which are determined by solving the corresponding gap equations. It is further shown that because of a certain asymmetry appearing in the energy dispersion relations corresponding to the lowest Landau level (LLL), the thermodynamic potential consists of an anomalous term. As it is argued in [19, 20], the anomalous term leads to certain topological effects that include, among others, an anomalous nondissipative Hall current and an anomalous electric charge. Moreover, this phase is characterized by the formation of a hybridized propagating mode known as an axion-polariton, which has interesting astrophysical consequences discussed exten-

* hooman.mortazavi@physics.sharif.ir

† Corresponding author: sadooghi@physics.sharif.ir

sively in [21]. Recently, in [22], the phase diagram of the MDCDW phase was explored at finite temperatures and in the presence of uniform magnetic fields. It is shown that the MDCDW phase is favored at magnetic fields and temperatures compatible with neutron stars. In particular, at intermediate densities, where a remnant mass is formed, the spatial modulation increases. This opens the possibility for this phase to be a favorable candidate for the quark matter in neutron stars.

In addition to high densities and large magnetic fields, neutron stars are also characterized by relatively large angular velocities of about $\Omega_{\max} \sim 10^3$ Hz. This leads to a linear velocity $\sim 10^{-2}c - 10^{-1}c$, where c is the light velocity. It is the purpose of this paper, to study the effect of rotation on the formation of the MDCDW phase. We assume that the magnetic field and angular velocity are uniform. This is only possible for cold neutron stars which are expected to rotate uniformly [23]. This assumption justifies another assumption concerning the temperature in this paper: Here, in contrast to [22], we neglect the effect of temperature and its possible interplay with high densities, magnetic fields, and rotations on the formation/suppression of the MDCDW phase in a cold quark matter.

As it is argued in [24, 25], a certain interplay between the effect of rotation and the magnetic field destroys chiral condensates. An effect which is referred to as “rotational magnetic inhibition” [24] or “inverse magnetorotational catalysis” (IMRC) [25]. For the MDCDW phase, the consequence of this effect would be a vanishing of the spatial modulation condensate, as a result of a certain correlation between two condensates in this phase. In this paper, we show that this indeed happens. A fact that may rule out this phase to be favorable for quark matter in rotating, dense, magnetized, and cold neutron stars. We emphasize that the present work is a natural extension of [22], where it is argued that the MDCDW phase is “viable candidate for the matter of neutron stars” [22]. Particularly in this context, we show that the inclusion of rotation to the condition imposed on the model used in [22] suppresses the formation of the MDCDW phase. It is not clear how robust the conclusions presented in [22] as well as those in the present paper, are in a more realistic model of a neutron star, where certain conditions, like β -equilibrium, isospin symmetry, and charge neutrality have to be imposed [26].

The organization of this paper is as follows: In Sec. II, we start with the Lagrangian density of a two-flavor NJL model with $U(1)_L \times U(1)_R \times SO(2) \times R^3$ symmetry in the presence of a background magnetic field and introduce the rotation by implementing an angular velocity parallel to the magnetic field in the Hamiltonian of the model. Then, defining two inhomogeneous condensates, we introduce the mass and spatial modulation condensates. We then solve the energy eigenvalue equation and determine, in particular, the energy eigenvalues and eigenfunctions in a cylindrical coordinate system. The solution to the Dirac equation in a rotating fermionic system with an without boundary conditions,

in the absence and/or presence of uniform magnetic fields is studied in [27–30], apart from [24, 25]. In the present paper, we neglect the effect of boundary conditions. In Sec. III, we determine the thermodynamic (one-loop effective) potential at finite temperature and density, and in the presence of constant magnetic fields. In particular, we focus on the low temperature limit as in [18] and explore the effect of rotation on the anomalous part of the effective potential. Having the thermodynamic potential at hand, it can be minimized with respect to two condensates. In Sec. IV A, we present our numerical results for the dependence of mass and spatial modulation condensates on the chemical potential μ , magnetic field eB and linear velocity ΩR , with Ω the angular velocity and R the radius. The results confirm the fact that rotation destroys both condensates as a consequence of the IMRC effect. Moreover, it is shown that for $\mu = 0$, the role of μ is played by a pure rotation in interplay with a background magnetic field. In Sec. IV B, we then explore the eB - μ , eB - ΩR , and μ - ΩR phase diagrams to study the impact of the IMRC effect on various phases appearing in the model. We conclude our results in Sec. V.

II. THE MODEL

To study the MDCDW phase in a rotating and dense medium, we start with the Lagrangian density of a two-flavor gauged NJL model,

$$\mathcal{L} = \bar{\psi}[i\cancel{D} - m_0]\psi + G[(\bar{\psi}\psi)^2 + (\bar{\psi}i\gamma^5\boldsymbol{\tau}\psi)^2], \quad (\text{II.1})$$

where $\psi^T = (u, d)$, $m_0 \equiv m_u = m_d$ is the up and down quark bare mass, and G the dimensionful NJL coupling constant. In what follows, we set $m_0 = 0$. Assuming a rigid rotation about the z direction with the angular velocity Ω , and a magnetic field aligned in the same direction, the operator \cancel{D} in (II.1) reads¹,

$$\cancel{D} = \gamma^0(\partial_t - i\Omega J_z) + \gamma^1\partial_x + \gamma^2\partial_y + \gamma^3\partial_z + ieQ\gamma^\mu A_\mu, \quad (\text{II.2})$$

with $e > 0$. Plugging the charge matrix $Q \equiv \text{diag}(q_u, q_d) = \text{diag}(2/3, -1/3)$ and the symmetric gauge $A_\mu = (0, -\mathbf{A}) = (0, By/2, -Bx/2, 0)$ into (II.2), we arrive at

$$\cancel{D}_f = \gamma^0(\partial_t - i\Omega J_z) + \gamma^1(\partial_x + iq_f eBy/2) + \gamma^2(\partial_y - iq_f eBx/2) + \gamma^3\partial_z, \quad (\text{II.3})$$

where the subscript $f = (u, d)$ denotes the two chosen flavors in this model. In this way, the magnetic field $\mathbf{B} = B\hat{z}$ with $B > 0$ is also aligned in the z direction.

¹ To derive \cancel{D} in (II.2), we follow exactly the same steps as in [24, 25, 29, 30].

The Dirac γ matrices in (II.2) and (II.3) are defined in the Weyl representation

$$\gamma^0 = \begin{pmatrix} 0 & 1 \\ 1 & 0 \end{pmatrix}, \quad \boldsymbol{\gamma} = \begin{pmatrix} 0 & \boldsymbol{\tau} \\ -\boldsymbol{\tau} & 0 \end{pmatrix}, \quad \gamma^5 = \begin{pmatrix} -1 & 0 \\ 0 & +1 \end{pmatrix}, \quad (\text{II.4})$$

with the Pauli matrices $\boldsymbol{\tau} = (\tau_1, \tau_2, \tau_3)$. Moreover, the total angular momentum in the z direction is given by $J_z \equiv L_z + \Sigma_z/2$ with $L_z = -i(x\partial_y - y\partial_x)$, and $\Sigma_z \equiv \mathbb{I}_{2 \times 2} \otimes \tau_3$.

As is described in [12], the MDCDW phase at finite baryon density is characterized by two nonlocal condensates

$$\langle \bar{\psi}\psi \rangle = \Delta \cos(\boldsymbol{q} \cdot \boldsymbol{x}), \quad \langle \bar{\psi}i\gamma^5\tau_3\psi \rangle = \Delta \sin(\boldsymbol{q} \cdot \boldsymbol{x}), \quad (\text{II.5})$$

with $\Delta = \text{const}$ and $\boldsymbol{q} \cdot \boldsymbol{x} \equiv \boldsymbol{q}_\mu x^\mu$. For simplicity, we assume that the modulation vector is aligned along the magnetic field direction \boldsymbol{z} , $\boldsymbol{q}^\mu = (0, 0, 0, 2b)$ [12, 18]. Expanding $(\bar{\psi}\psi)^2$ and $(\bar{\psi}i\gamma^5\tau_3\psi)^2$ in the interacting part of the Lagrangian (II.1) around their mean fields (II.5), we arrive first at the semi-bosonized Lagrangian

$$\mathcal{L}_{\text{MF}} = \bar{\psi}[i\not{\mathbb{M}} - me^{-2i\gamma^5\tau_3\theta}]\psi - \frac{m^2}{4G}, \quad (\text{II.6})$$

where the dynamical mass $m \equiv -2G\Delta$, with Δ given in (II.5) and $\theta \equiv bz$. Performing at this stage a local chiral transformation as in [12, 18]

$$\psi \rightarrow e^{+i\gamma^5\tau_3\theta}\psi, \quad \bar{\psi} \rightarrow \bar{\psi}e^{+i\gamma^5\tau_3\theta}, \quad (\text{II.7})$$

we arrive at

$$\mathcal{L}_{\text{MF}} = \bar{\psi}[i\not{\mathbb{M}}_f - m + b\gamma^5\tau_3]\psi - \frac{(m)^2}{4G}. \quad (\text{II.8})$$

Here, we used $\not{\partial}\theta = \gamma^3 b$. Plugging τ_3 into (II.8), we obtain the corresponding Lagrangian density for each flavor \mathcal{L}_f ,

$$\mathcal{L}_{\text{MF}} = \sum_{f=\{u,d\}} \mathcal{L}_f, \quad (\text{II.9})$$

with

$$\mathcal{L}_f = \bar{\psi}_f (i\not{\mathbb{M}}_f - m + s_f b\gamma^5\tau_3) \psi_f. \quad (\text{II.10})$$

Here, \mathbb{M}_f is defined in (II.3) and $s_f \equiv \text{sign}(q_f)$ is given by $(s_u, s_d) = (+1, -1)$ for up and down quarks, respectively. To determine the energy spectrum of this model, we solve the energy eigenfunction equation,

$$\mathcal{H}_f \psi_f = E_f \psi_f, \quad (\text{II.11})$$

with the Hamiltonian for each flavor f ,

$$\mathcal{H}_f \equiv i\boldsymbol{\gamma} \cdot \boldsymbol{\Pi}_f + m\gamma^0 - s_f b\gamma^0\gamma^5\tau_3. \quad (\text{II.12})$$

Here, $\boldsymbol{\gamma} \cdot \boldsymbol{\Pi}_f$ includes the spatial part of Π_f^μ , defined in (II.3). Following the method presented in App. A, the corresponding energy eigenvalues to the lowest and higher Landau levels (LLL and HLL) read:

- For LLL ($n = 0$), we obtain

$$E_f^{n=0} = -\Omega j + b + \epsilon\sqrt{p_z^2 + m^2}, \quad (\text{II.13})$$

with $\epsilon = \pm 1$.

- For HLL ($n > 0$), we obtain

$$E_f^{n>0} = -\Omega j + \zeta \left[\left(b + \epsilon\sqrt{p_z^2 + m^2} \right)^2 + 2n|q_f eB| \right]^{1/2}, \quad (\text{II.14})$$

with $\epsilon = \pm 1$, $\zeta = \pm 1$, and $n = 1, 2, 3, \dots$. Moreover, $j \equiv \ell + 1/2$ is the eigenvalue of the J_z operator. The latter commutes with \mathcal{H}_f , and has simultaneous eigenfunctions with this operator. Comparing (II.14) with the energy eigenvalues of the same model without rotation $E_f^{n,\Omega=0}$ in [12], it turns out that $E_f^{n,\Omega=0} - \Omega j = E_f^n$. In what follows, we determine the thermodynamic potential of this model.

III. THE THERMODYNAMIC POTENTIAL

To determine the thermodynamic potential of the MDCDW model at finite temperature T and chemical potential μ , let us start with

$$V_{\text{eff}} = -\frac{1}{V} \ln Z, \quad (\text{III.1})$$

where V is the four-dimensional space-time volume, and the partition function Z is given by

$$Z = \int \mathcal{D}\bar{\psi}\mathcal{D}\psi \exp\left(-i \int d^4x \mathcal{L}_{\text{MF}}\right), \quad (\text{III.2})$$

with the mean-field Lagrangian

$$\mathcal{L}_{\text{MF}} = \frac{m^2}{4G} - \bar{\psi} (i\not{\mathbb{M}} - m + b\gamma^5\tau_3 + \mu\gamma^0) \psi, \quad (\text{III.3})$$

that, comparing to \mathcal{L}_{MF} from (II.8), we have introduced μ and neglect the current mass m_0 . Using then the definition of the Hamiltonian \mathcal{H}_f from (II.12), V_{eff} is first given by

$$V_{\text{eff}} = \frac{m^2}{4G} + V_{\text{eff}}^{(1)},$$

with

$$V_{\text{eff}}^{(1)} \equiv -\frac{1}{V} \text{Tr}_{\text{sfc}} \{ \ln[i\partial_0 - (\mathcal{H}_f - \mu)] \}, \quad (\text{III.4})$$

where the trace is to be built over the spin (s), flavor (f), and color (c) degrees of freedom. To do this, we consider,

as in [24], a cylindrical volume with L_z , the length of the cylinder, and R , its radius. Assuming as in [24] that the maximum of $\psi(\boldsymbol{\rho}, \boldsymbol{\varphi}, z)$ is inside the cylinder, it is possible to determine an upper bound for the summation over ℓ (see the Appendix of [24]). This leads to the following phase space for the positively and negatively charged quarks in a rotating medium

$$\left\{ \begin{array}{l} \frac{L_z}{V} \sum_{n=0}^{\infty} \sum_{\ell=-n}^{\mathcal{N}_u-n-1} \int \frac{dp_z}{2\pi} \quad \text{for } f = u, \\ \frac{L_z}{V} \sum_{n=0}^{\infty} \sum_{\ell=-\mathcal{N}_d+n}^{n-1} \int \frac{dp_z}{2\pi} \quad \text{for } f = d. \end{array} \right. \quad (\text{III.5})$$

Here, n and ℓ are the quantum numbers corresponding to Landau levels and rotation, respectively. Moreover, \mathcal{N}_f , the Landau degeneracy factor for each flavor $f = \{u, d\}$ is defined by

$$\mathcal{N}_f \equiv \lfloor \frac{|q_f e B| S}{2\pi} \rfloor. \quad (\text{III.6})$$

Here, $S = \pi R^2$. Using the replacement

$$p_0 \rightarrow i\omega_k \equiv i\pi T(2k+1), \quad \text{and} \quad \int \frac{dp_0}{2\pi} \rightarrow iT \sum_{k=-\infty}^{+\infty}, \quad (\text{III.7})$$

and performing the summation over the Matsubara frequencies ω_k by making use of

$$\frac{1}{\beta} \sum_k [\omega_k^2 + (E - \mu)^2] = |E - \mu| + \frac{2}{\beta} \ln \left(1 + e^{-\beta|E - \mu|} \right), \quad (\text{III.8})$$

with $\beta \equiv T^{-1}$, we arrive at the thermodynamic potential at finite T and μ ,

$$V_{\text{eff}} = \frac{m^2}{4G} - \frac{N_c}{4\pi S} \sum_f \sum_{(n), \ell} \times \int_{-\infty}^{+\infty} dp_z \left\{ |E_f^n - \mu| + \frac{2}{\beta} \ln \left(1 + e^{-\beta|E_f^n - \mu|} \right) \right\}, \quad (\text{III.9})$$

where

$$\sum_{(n)} \equiv \sum_{n=0, \epsilon} + \sum_{n>0, \zeta, \epsilon}, \quad (\text{III.10})$$

and N_c is the number of colors, and E_f^n for $n = 0$ and $n > 0$ are given in (II.13) and (II.14), respectively. Similar to [18], we separate $V_{\text{eff}}^{(1)}$ into the zero T part, $V_{T=0}$, the part including μ and Ω , $V_{\mu, \Omega}$, and the finite T part, $V_{T \neq 0}$,

$$V_{\text{eff}}^{(1)} = V_{T=0} + V_{\mu, \Omega} + V_{T \neq 0}, \quad (\text{III.11})$$

with

$$\begin{aligned} V_{T=0} &= -\frac{N_c}{4\pi S} \sum_f \sum_{(n), \ell} \int dp_z |E_f^n + \Omega j|, \\ V_{\mu, \Omega} &= -\frac{N_c}{4\pi S} \sum_f \sum_{(n), \ell} \int dp_z (|E_f^n - \mu| - |E_f^n + \Omega j|), \\ V_{T \neq 0} &= -\frac{N_c T}{2\pi S} \sum_f \sum_{(n), \ell} \int dp_z \ln[1 + e^{-\beta|E_f^n - \mu|}]. \end{aligned} \quad (\text{III.12})$$

In what follows, we consider only the $T \rightarrow 0$ case. Using

$$\lim_{T \rightarrow 0} T \ln(1 + e^{-\beta x}) = -x\theta(-x),$$

the $V_{T \neq 0}$ vanishes. We thus focus on $V_{T=0}$ and $V_{\mu, \Omega}$ in (III.12). Similar to the nonrotating case, $V_{T=0}$ has to be appropriately regularized. According to the definition of E_f^n from (II.13) and (II.14), $E_f^n + \Omega j = E_f^{\Omega=0}$ is independent of $j = \ell + 1/2$ (or equivalently ℓ). A summation over ℓ is therefore possible, and leads to a factor \mathcal{N}_f , defined in (III.6). The zero T part of the potential is thus given by

$$V_{T=0} = -\frac{N_c}{4\pi S} \sum_f \mathcal{N}_f \sum_{(n)} \int dp_z |E_f^{n, \Omega=0}|. \quad (\text{III.13})$$

Apart from the factor \mathcal{N}_f/S , this is the same integral that appears also in [18, 22]. Using the same proper-time regularization as in [18, 22], it reads

$$V_{T=0} = \frac{N_c}{S} \sum_f \mathcal{N}_f \sum_{(n)} \int dp_z \int_{\frac{1}{\Lambda^2}}^{\infty} \frac{ds}{(4\pi s)^{3/2}} e^{-s(E_f^{n, \Omega=0})^2}. \quad (\text{III.14})$$

Here, Λ is a cutoff regulator. It is possible to perform the summation over Landau levels n and ζ as well as ϵ . Using

$$1 + 2 \sum_{n=1}^{\infty} e^{-2An} = \coth(A), \quad (\text{III.15})$$

the final expression for $V_{T=0}$, is given by

$$\begin{aligned} V_{T=0} &= \frac{N_c}{S} \sum_{f=\{u, d\}} \mathcal{N}_f \int dp_z \int_{\frac{1}{\Lambda^2}}^{\infty} \frac{ds}{(4\pi s)^{3/2}} \\ &\times \sum_{\epsilon=\pm 1} e^{-s(b+\epsilon\sqrt{p_z^2+m^2})^2} \coth(s|q_f e B|). \end{aligned} \quad (\text{III.16})$$

Let us now consider $V_{\mu, \Omega}$ from (II.12). To regularize it, we use as in [18], a cutoff regularization by introducing a Heaviside θ as a function of the regulator Λ'

$$\begin{aligned} V_{\mu, \Omega} &= -\frac{N_c}{4\pi S} \sum_{f, (n), \ell} \int_{-\infty}^{+\infty} dp_z \\ &\times (|E_f^n - \mu| - |E_f^n + \Omega j|) \theta(\Lambda' - |E_f^n + \Omega j|). \end{aligned} \quad (\text{III.17})$$

To evaluate $V_{\mu,\Omega}$, it is necessary to separate it into two parts, corresponding to LLL and HLLs, $n = 0$ and $n > 0$,

$$V_{\mu,\Omega} = \mathcal{V}_{\mu,\Omega}^{n=0} + \mathcal{V}_{\mu,\Omega}^{n>0}, \quad (\text{III.18})$$

with

$$\begin{aligned} \mathcal{V}_{\mu,\Omega}^{n=0} &\equiv -\frac{N_c}{4\pi S} \sum_{f,\ell,\epsilon} \int_{-\infty}^{+\infty} dp_z \theta \left(\Lambda' - |E_f^{n=0,\Omega=0}| \right) \left(|E_f^{n=0} - \mu| - |E_f^{n=0,\Omega=0}| \right), \\ \mathcal{V}_{\mu,\Omega}^{n>0} &\equiv -\frac{N_c}{4\pi S} \sum_{f,\ell,\zeta,\epsilon,n>0} \int_{-\infty}^{+\infty} dp_z \theta \left(\Lambda' - |E_f^{n>0,\Omega=0}| \right) \left(|E_f^{n>0} - \mu| - |E_f^{n>0,\Omega=0}| \right). \end{aligned} \quad (\text{III.19})$$

Let us first consider the LLL contribution to the effective potential, $\mathcal{V}_{\mu,\Omega}^{n=0}$. Following the procedure described in [18], we arrive first at

$$\mathcal{V}_{\mu,\Omega}^{n=0} = -\frac{N_c}{4\pi S} \sum_{f,\ell,\epsilon} \int_{-\infty}^{+\infty} dp_z \left(|E_f^{n=0} - \mu| - |E_f^{n=0,\Omega=0}| \right) - \frac{N_c b}{\pi S} \sum_{f,\ell} (\Omega j + \mu). \quad (\text{III.20})$$

For numerical purposes, it is necessary to sum over ϵ and perform the integration over p_z in the first term of $\mathcal{V}_{\mu,\Omega}^{n=0}$. To do this, we use the method described in [18], and arrive after some work at²

$$\mathcal{V}_{f,\ell} \equiv \sum_{\epsilon} \int_{-\infty}^{+\infty} dp_z \left(|E_f^{n=0} - \mu| - |E_f^{n=0,\Omega=0}| \right) = \begin{cases} 0 & |a_2| < |a_1| < |m|, \\ -4I(0, P_{a_1}) + 4|a_1|P_{a_1} & |a_2| < |m| < |a_1|, \\ 4I(P_{a_1}, P_{a_2}) + 4|a_1|P_{a_1} - 4|a_2|P_{a_2} & |m| < |a_2| < |a_1|, \\ 0 & |a_1| < |a_2| < |m|, \\ 4I(0, P_{a_2}) - 4|a_2|P_{a_2} & |a_1| < |m| < |a_2|, \\ 4I(P_{a_1}, P_{a_2}) + 4|a_1|P_{a_1} - 4|a_2|P_{a_2} & |m| < |a_1| < |a_2|, \end{cases} \quad (\text{III.21})$$

with $a_1 \equiv b - \Omega j - \mu$, $a_2 \equiv b$, $P_{a_i} = \sqrt{a_i^2 - m^2}$, $i = 1, 2$, and $I(\Lambda_1, \Lambda_2)$ defined in (B.5). The second term in (III.20), is the well-known anomalous potential, $\mathcal{V}_{\text{anomal}}$ [12, 18],

$$\mathcal{V}_{\text{anomal}} \equiv -\frac{N_c b}{\pi S} \sum_{f,\ell} (\Omega j + \mu). \quad (\text{III.22})$$

Having in mind that $j = \ell + 1/2$, and performing the summation over f and ℓ according to (III.5), we have

$$2 \sum_{f,\ell} (\Omega j + \mu) = [2(\mathcal{N}_u + \mathcal{N}_d) \mu + (\mathcal{N}_u^2 - \mathcal{N}_d^2) \Omega]. \quad (\text{III.23})$$

The anomalous potential is thus given by

$$\mathcal{V}_{\text{anomal}} = -\frac{N_c b}{2\pi S} [2(\mathcal{N}_u + \mathcal{N}_d) \mu + (\mathcal{N}_u^2 - \mathcal{N}_d^2) \Omega]. \quad (\text{III.24})$$

Let us notice that for $\Omega = 0$, the result for $\mathcal{V}_{\text{anomal}}$ coincides with the anomalous part of the effective potential

presented in [12]. According to the above results, after an appropriate cutoff regularization, the LLL contribution to the effective potential $V_{\mu,\Omega}$ is thus given by

$$\mathcal{V}_{\mu,\Omega}^{n=0} = -\frac{N_c}{4\pi S} \sum_{f,\ell} \mathcal{V}_{f,\ell} + \mathcal{V}_{\text{anomal}}, \quad (\text{III.25})$$

where $\mathcal{V}_{f,\ell}$ is given in (III.21) and $\mathcal{V}_{\text{anomal}}$ in (III.24).

Let us now consider the HLL contribution to the effective potential, $\mathcal{V}_{\mu,\Omega}^{n>0}$ from (III.19). We simplify this expression step by step for our numerical purposes. Using the definition of $E_f^{n>0} = -\Omega j + \zeta E_+$ with

$$E_+ \equiv \left[\left(b + \epsilon \sqrt{p_z^2 + m^2} \right)^2 + 2n|q_f e B| \right]^{1/2}, \quad (\text{III.26})$$

from (II.14), the summation over ζ leads to

$$\begin{aligned} &\sum_{\zeta=\pm 1} \left(|E_f^{n>0} - \mu| - |E_f^{n>0,\Omega=0}| \right) \\ &= 2(|\mu + \Omega j| - E_+) \theta(|\mu + \Omega j| - E_+) \theta(\Lambda' - E_+). \end{aligned} \quad (\text{III.27})$$

Plugging this expression into $\mathcal{V}_{\mu,\Omega}^{n>0}$ from (III.19), it is

² In App. B.1, we outline the derivation of (III.21).

given by

$$\mathcal{V}_{\mu,\Omega}^{n>0} = -\frac{N_c}{2\pi S} \sum_{f,\epsilon} \sum_{n=1}^{N_{\max}} \int_{-\infty}^{+\infty} dp_z \sum_{k=0}^{N_f-1} \mathcal{I}_{f,\epsilon,n,k}(p_z), \quad (\text{III.28})$$

with

$$N_{\max} \equiv \left\lfloor \frac{\Lambda'^2 - \left(b + \epsilon \sqrt{p_z^2 + m^2}\right)^2}{2|q_f eB|} \right\rfloor, \quad (\text{III.29})$$

which results from $\theta(\Lambda' - E_+)$, and

$$\mathcal{I}_{f,\epsilon,n,k} \equiv (|\mu_f + \Omega k| - E_+) \theta(|\mu_f + \Omega k| - E_+) \times \theta(\Lambda' - E_+). \quad (\text{III.30})$$

Here, μ_f for $f = \{u, d\}$ are defined by

$$\begin{aligned} \mu_u &\equiv \mu - \Omega \left(n - \frac{1}{2} \right), \\ \mu_d &\equiv \mu + \Omega \left(n - N_d + \frac{1}{2} \right). \end{aligned} \quad (\text{III.31})$$

They arise by an appropriate redefinition of the summation over ℓ for two different flavors in (III.5). After performing the summation over k in (III.28), we arrive finally at

$$\mathcal{V}_{\mu,\Omega}^{n>0} = -\frac{N_c}{2\pi S} \sum_{f,\epsilon} \sum_{n=1}^{N_{\max}} \int_{-\infty}^{+\infty} dp_z \mathcal{K}_{f,\epsilon,n}(p_z), \quad (\text{III.32})$$

where $\mathcal{K}_{f,\epsilon,n}(p_z)$ is a lengthy conditional expression, presented in Appendix B 2. To summarize, $V_{\text{eff}}^{(1)}$ at zero temperature and finite density is thus given by

$$V_{\text{eff}}^{(1)} = V_{T=0} + V_{\mu,\Omega} = V_{T=0} + \mathcal{V}_{\mu,\Omega}^{n=0} + \mathcal{V}_{\mu,\Omega}^{n>0},$$

with $V_{T=0}$ given in (III.16), $\mathcal{V}_{\mu,\Omega}^{n=0}$ in (III.25), and $\mathcal{V}_{\mu,\Omega}^{n>0}$ in (III.32). In what follows, we use this effective potential to study the effect of rotation on a dense and magnetized quark matter in the MDCDW phase.

IV. NUMERICAL RESULTS

As it is shown in the previous section, the effective potential of a MDCDW medium at zero temperature, finite density, and in the presence of rotation is given by $V_{\text{eff}}^{(1)} = V_{T=0} + V_{\mu,\Omega}$. The regularized expression for $V_{T=0}$, presented in (III.14), does not depend on μ and Ω , but depends through $E_f^{n,\Omega=0}$ on m and b . These are taken as two dynamical variables in this context. The part of the potential including μ and Ω is separated into two parts: The LLL contribution $\mathcal{V}_{\mu,\Omega}^{n=0}$, presented in (III.25) includes, in particular, the anomalous potential $\mathcal{V}_{\text{anomalous}}$

from (III.24). This part, together with the HLL contribution $\mathcal{V}_{\mu,\Omega}^{n>0}$, presented in (III.32) depend explicitly on m and b . To study the effect of μ, eB and Ω on the formation of these two dynamical variables, we have to determine the global minima of V_{eff} with respect to m and b . To do this, we performed a numerical computation in the regime $\mu \in [0, 0.8]$ GeV, $\sqrt{eB} \in [0, 0.8]$ GeV, corresponding to $eB \in [0, 0.64]$ GeV², and the linear velocity $\Omega R \in [0, 0.1]$. To convert the values of Ω and eB to Hertz (Hz) and Gauss (G), we use 1 GeV = 1.52×10^{24} Hz and $eB = 1$ GeV² corresponding to $B \sim 1.7 \times 10^{20}$ G.

The main purpose of the present paper, is to answer the question of whether the MDCDW phase survives the extreme conditions of cold neutron stars. In particular, what is the effect of rotation on the formation/suppression of this phase in these extreme conditions? In this regard, let us notice that the maximum radius of a neutron star $R_{\max} \sim 10$ km, its maximum angular velocity $\Omega_{\max} \sim 10^3$ Hz [24]. These lead to a maximum linear velocity $(\Omega R)_{\max} \sim 3 \times 10^{-2}c$. As concerns the magnetic field of a neutron star, its maximum value is $B_{\max} \sim 10^{17}$ G [31], which corresponds to $\sqrt{eB} \sim 0.02$ GeV. The chosen intervals for μ, eB , and ΩR are thus quite relevant to study the effect of rotation on the MDCDW phase in cold, magnetized and rotating neutron stars. In what follows, we work with dimensionless quantities. To do this, all dimensionful variables are rescaled with $\Lambda = 1$ GeV. We work, as in [24], with $R = 10^3 \Lambda^{-1}$, and set, whenever necessary $G\Lambda^2 = 6$ [18], and $\Lambda' = 10\Lambda$ [18].

In Sec. IV A, we present our numerical results for the μ, \sqrt{eB} , and ΩR dependencies of m and b for different fixed values of $\Omega R, \sqrt{eB}$, and μ . In Sec. IV B, we then present the corresponding phase portraits to $\sqrt{eB}-\mu, \sqrt{eB}-\Omega R$, and $\mu-\Omega R$.

A. The effects of μ, eB and Ω on the chiral condensate m and spatial modulation b

1. The μ dependence

In Fig. 1, the μ dependence of the chiral condensate m (solid orange) and spatial modulation b (dashed blue) is plotted for fixed values of ΩR and \sqrt{eB} . In each row ΩR is constant and \sqrt{eB} varies. In contrast, in each column \sqrt{eB} is constant and ΩR varies. The first to fourth rows correspond to $\Omega R = 0, 10^{-3}, 5 \times 10^{-3}$ and 10^{-2} , and the first to third columns correspond to $\sqrt{eB} = 0.15\Lambda, 0.25\Lambda$ and 0.45Λ . Let us first compare the plots in the first row. The result from Fig. 1(a) is comparable with the result presented in [22]. The four different regions described in [22] can also be identified in this plot. In the first region $\mu \lesssim 0.45\Lambda$, the chiral symmetry is broken, whereas the system is spatially symmetric ($b = 0$). In the second region, $0.45\Lambda \lesssim \mu \lesssim 0.6\Lambda$, m decreases, whereas b increases. The remnant mass is visible in a third region, $0.6\Lambda \lesssim \mu \lesssim 0.75\Lambda$. The spatial modulation b is nonvanishing and rather large in this regime. A fourth

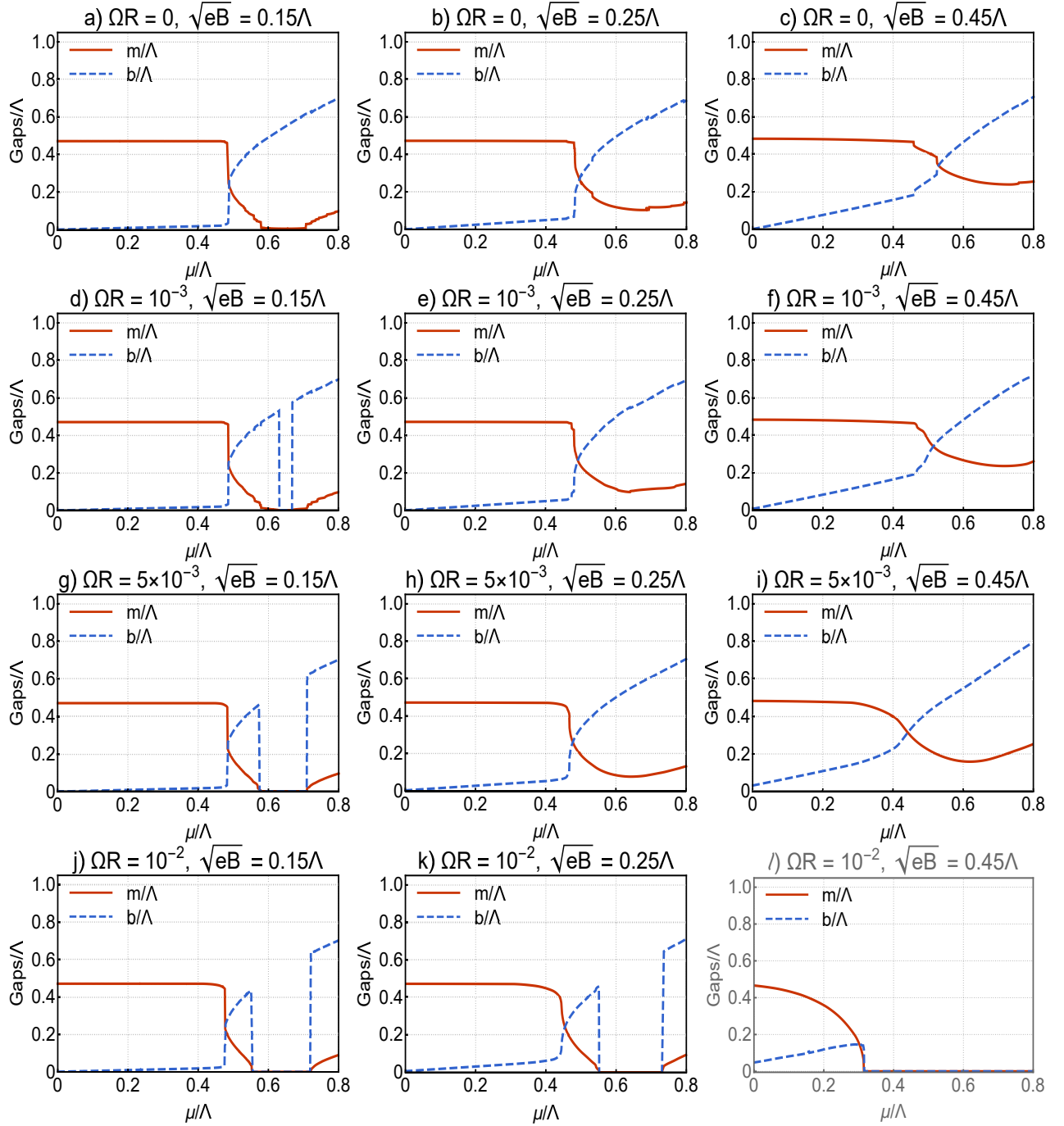


FIG. 1. color online. The μ dependence of the chiral condensate m and spatial modulation b are plotted for fixed values of ΩR and \sqrt{eB} . Solid orange and dashed blue curves correspond to m and b , respectively. In each row (column) ΩR s are constant (vary) and \sqrt{eB} s vary (are constant). First row (panels a, b, and c): $\Omega R = 0$ and $\sqrt{eB} = 0.15\Lambda, 0.25\Lambda, 0.45\Lambda$. Second row (panels d, e, and f): $\Omega R = 10^{-3}$ and $\sqrt{eB} = 0.15\Lambda, 0.25\Lambda, 0.45\Lambda$. Third row (panels g, h, and i): $\Omega R = 5 \times 10^{-3}$ and $\sqrt{eB} = 0.15\Lambda, 0.25\Lambda, 0.45\Lambda$. Fourth row (panels j, k, and l): $\Omega R = 10^{-2}$ and $\sqrt{eB} = 0.15\Lambda, 0.25\Lambda, 0.45\Lambda$.

region is visible in $\mu \gtrsim 0.75\Lambda$. In this regime m and b both increase with increasing μ .³ These four regimes

are visible in all the plots in the first column [Figs. 1(a),

³ Let us emphasize that Fig. 1(a) cannot be compared with Fig. 3(b) of [18], because as it is argued in [22], a very small rem-

nant mass $m \sim 5$ MeV in the intermediate regime of densities $0.6\Lambda \lesssim \mu \lesssim 0.75\Lambda$ is not considered in [18], and, consequently, b is reported to be zero in this regime.

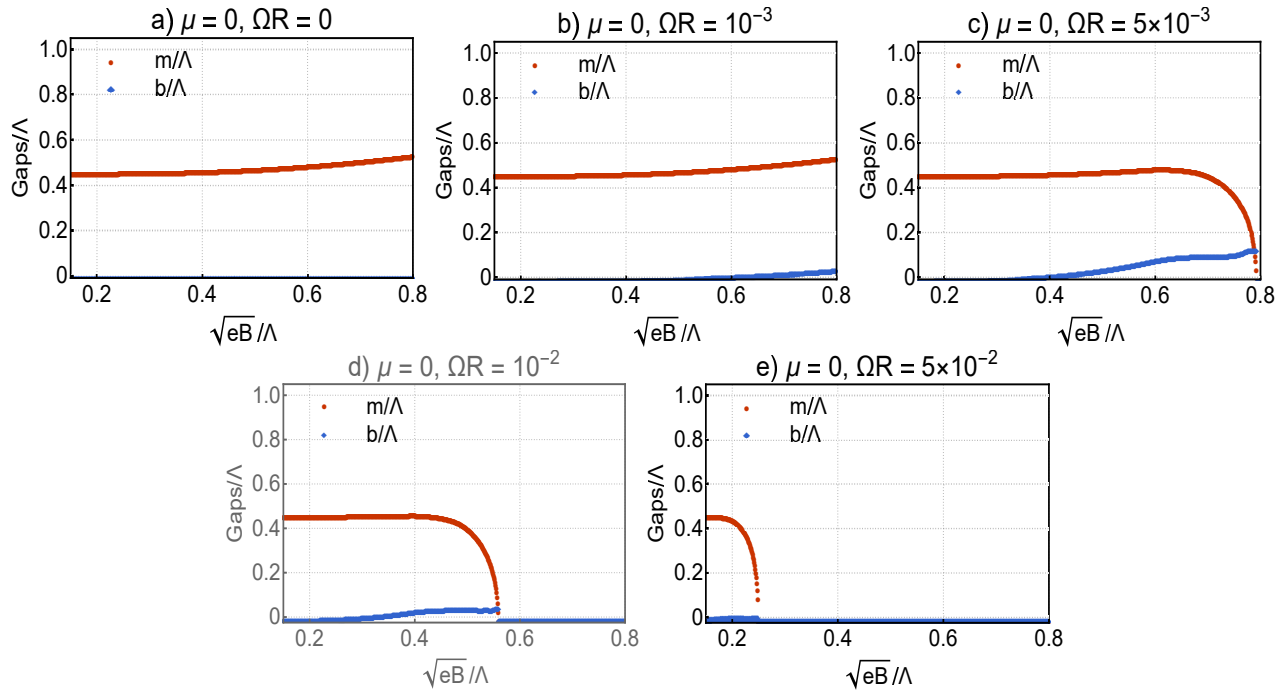


FIG. 2. color online. The dependence of the chiral condensate m and spatial modulation b on \sqrt{eB} is plotted for $\mu = 0$ and $\Omega R = 0, 10^{-3}, 5 \times 10^{-3}, 10^{-2}, 5 \times 10^{-2}$. Orange dots and blue diamonds correspond to m/Λ and b/Λ , respectively. It turns out that even for $\mu = 0$, the interplay between eB and ΩR leads to a finite b .

1(d), 1(g), and 1(j)], where $\sqrt{eB} = 0.15\Lambda$ is constant, and ΩR increases. Here, ΩR merely affects the production of m . It decreases (vanishes) by increasing ΩR . As it turns out, the remnant mass appearing in the third region, $0.6\Lambda \lesssim \mu \lesssim 0.75\Lambda$, disappears. Consequently, b also vanishes in this regime. This specific feature of ΩR in destroying the dynamical mass is expected from [24, 25]. As concerns the fourth regime, however, it turns out that the system reenters from a chirally symmetric homogeneous regime into a chiral symmetry broken phase for $\mu \gtrsim 0.75\Lambda$, where the spatial symmetry is also broken by a nonvanishing and rather large b .

By increasing \sqrt{eB} and for small values of ΩR , the remnant mass in the third region increases. This is expected from the magnetic catalysis, and is visible by comparing the plots in the second column [Figs. 1(b), 1(e), 1(h)], corresponding to $\sqrt{eB} = 0.25\Lambda$ with the ones in the third column [Figs. 1(c), 1(f), 1(i)], corresponding to $\sqrt{eB} = 0.45\Lambda$. Here, as it turns out, b increases also in the first region $\mu \lesssim 0.4\Lambda$. However, once ΩR is large enough, m vanishes in the third region because of the IMRC [25]. Larger ΩR destroys the dynamical mass even in the fourth regime $\mu \gtrsim 0.75\Lambda$ [see Fig. 1(l)] with $\Omega R = 10^{-2}$ and $\sqrt{eB} = 0.45\Lambda$. Hence, large enough ΩR does not allow any reentrance in the symmetry broken phase in the fourth regime $\mu \gtrsim 0.75\Lambda$. In IV B, we study the effect of eB and ΩR on the critical values of μ .

2. The eB dependence

In Fig. 2, the eB dependence of the chiral condensate m (orange dots) and spatial modulation b (blue diamonds) is plotted for $\mu = 0$ and $\Omega R = 0, 10^{-3}, 5 \times 10^{-3}, 10^{-2}, 5 \times 10^{-2}$. As expected for $\mu = 0$ and $\Omega R = 0$, the dynamical mass increases slightly with increasing eB , and $b = 0$ [Fig. 2(a)]. For a nonvanishing $\Omega R = 0.001$, however, b increases slightly with increasing eB [Fig. 2(b)], and for $\Omega R = 0.005$, because of the onset of the IMRC effect, m decreases in the regime $\sqrt{eB} \gtrsim 0.7\Lambda$. The spatial modulation b , however, increases with increasing eB [see Fig. 2(c)]. We conclude therefore that even for $\mu = 0$, a certain interplay between eB and ΩR leads to a finite b . This is indeed expected because of the similarity between μ and ΩR discussed in [24].

For larger values of ΩR , the rotation completely destroys m , and for vanishing m , the spatial modulation b also vanishes [Figs. 2(d) and 2(e)]. For $\Omega R \gtrsim 0.005$, the transition from the MDCDW phase with $m, b \neq 0$ to the symmetry restored phase with $m = 0$ is of first order [see Fig. 6(a)]. By comparing the plots from Figs. 2(c)-2(e), it turns out that the critical value of eB , for which m and b vanish, decreases with increasing ΩR . This result coincides with the results presented in the phase diagram eB - ΩR in Fig. 6.

To study the effect of μ on the above scenario, the eB dependence of the chiral condensate m (solid orange) and spatial modulation b (dashed blue) is plotted for fixed values of ΩR and nonvanishing μ in Fig. 3. In each row ΩR is constant and μ varies. In contrast, in each column

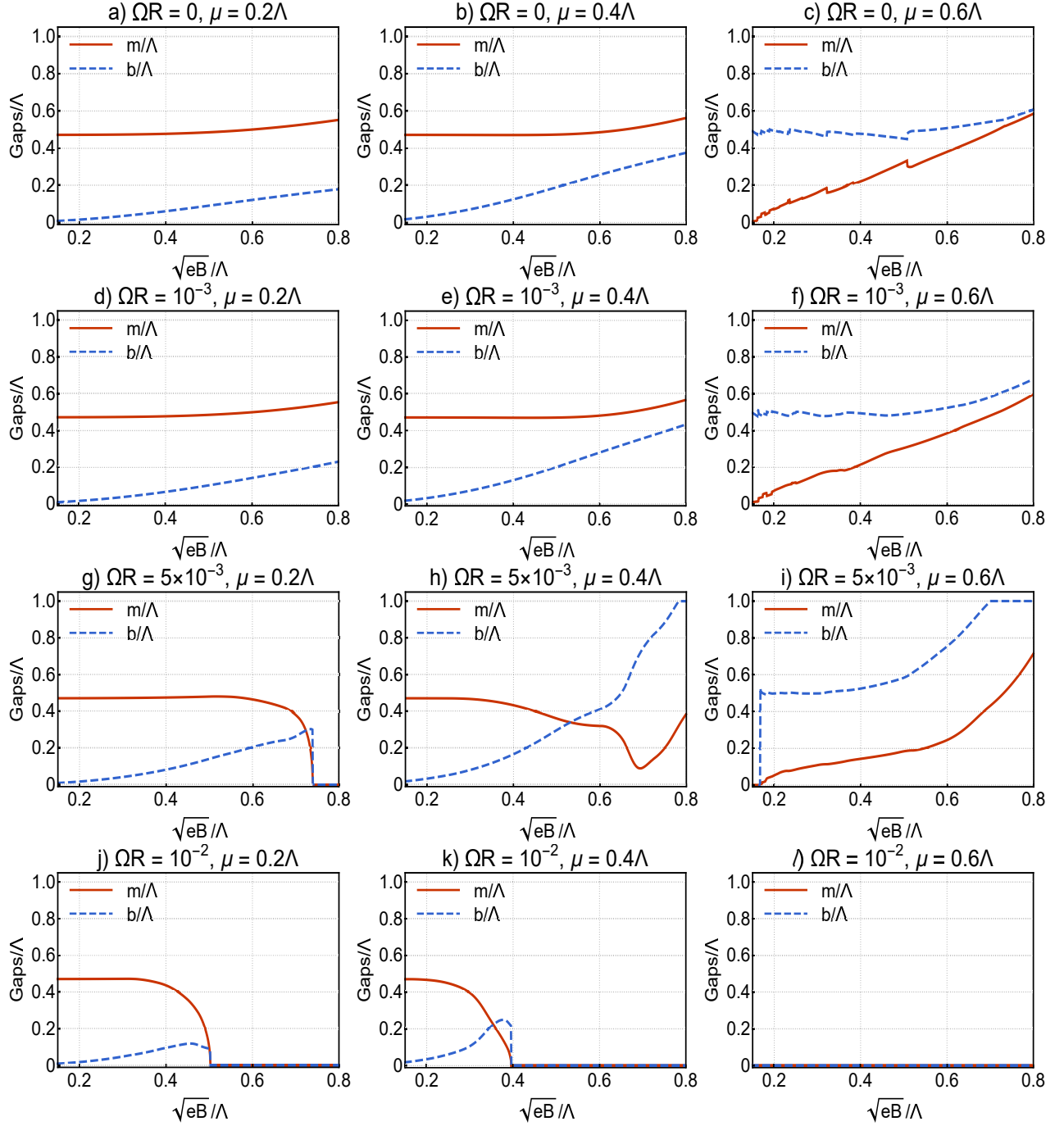


FIG. 3. color online. The dependence of the chiral condensate m and spatial modulation b on \sqrt{eB} is plotted for fixed values of ΩR and μ . Solid orange and dashed blue curves correspond to m and b , respectively. In each row (column) ΩR s are constant (vary) and μ s vary (are constant). First row (panels a, b, and c): $\Omega R = 0$ and $\mu = 0.2\Lambda, 0.4\Lambda, 0.6\Lambda$. Second row (panels d, e, and f): $\Omega R = 10^{-3}$ and $\mu = 0.2\Lambda, 0.4\Lambda, 0.6\Lambda$. Third row (panels g, h, and i): $\Omega R = 5 \times 10^{-3}$ and $\mu = 0.2\Lambda, 0.4\Lambda, 0.6\Lambda$. Fourth row (panels j, k, and l): $\Omega R = 10^{-2}$ and $\mu = 0.2\Lambda, 0.4\Lambda, 0.6\Lambda$. For the plots to be comparable, the range in the horizontal axis is chosen to be in the interval $\sqrt{eB} \in [0.15\Lambda, 0.8\Lambda]$.

μ is constant and ΩR varies. The first to fourth rows correspond to $\Omega R = 0, 10^{-3}, 5 \times 10^{-3}$ and 10^{-2} , and the first to third columns correspond to $\mu = 0.2\Lambda, 0.4\Lambda$, and 0.6Λ . It is possible to compare the results presented in Figs. 3(a)-3(c) with those from Fig. 2 of [18], where $\Omega R = 0$. To do this, one shall, however, be very cau-

tious because, according to [22] and also our results from Fig. 1, the small remnant mass at intermediate μ is not considered in [18]. Hence, by comparing, e.g. Fig. 3(c) for $\Omega R = 0$ and $\mu = 0.6\Lambda$ with Fig. 2(d) in [18], we observe that a remnant mass $m \sim 5 - 70$ MeV appears in the regime $\sqrt{eB} \leq 0.2\Lambda$ of Fig. 3(c), while this mass is

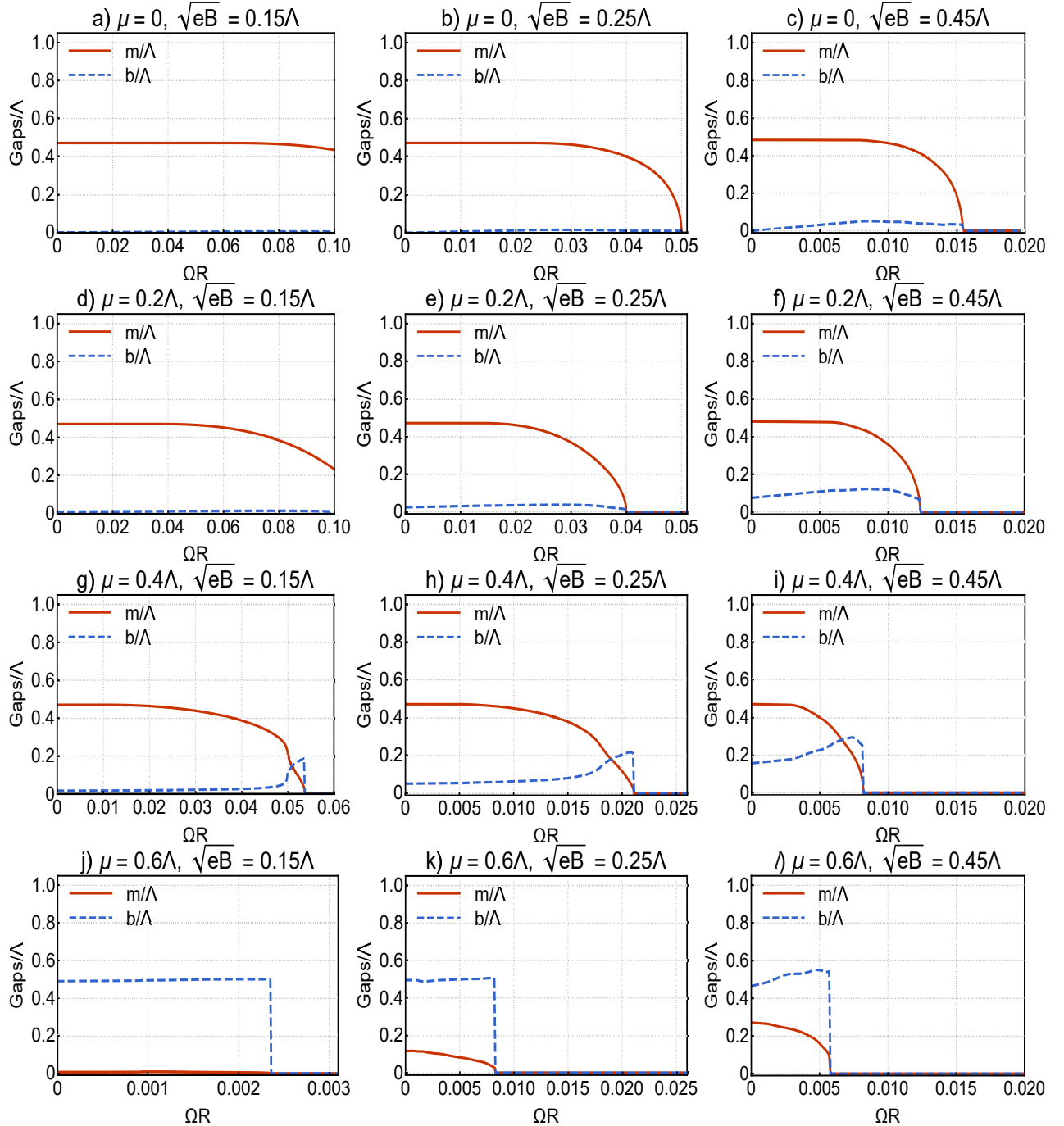


FIG. 4. color online. The ΩR dependence of the chiral condensate m and spatial modulation b are plotted for fixed values of \sqrt{eB} and μ . Solid orange and dashed blue curves correspond to m and b , respectively. First row (panels a, b, and c): $\mu = 0$ and $\sqrt{eB} = 0.15\Lambda, 0.25\Lambda, 0.45\Lambda$. Second row (panels d, e, and f): $\mu = 0.2\Lambda$ and $\sqrt{eB} = 0.15\Lambda, 0.25\Lambda, 0.45\Lambda$. Third row (panels g, h, and i): $\mu = 0.4\Lambda$ and $\sqrt{eB} = 0.15\Lambda, 0.25\Lambda, 0.45\Lambda$. Fourth row (panels j, k, and l): $\mu = 0.6\Lambda$ and $\sqrt{eB} = 0.15\Lambda, 0.25\Lambda, 0.45\Lambda$.

not considered in Fig. 2(d) of [18] in the same regime of $\sqrt{eB} \leq 0.2\Lambda$. Let us emphasize that the result from Fig. 3(c) is consistent with Fig. 1(a) for $\Omega R = 0$, which is by itself in complete agreement with the result presented in [22].

The plots presented in the first column of Fig. 3 [Figs. 3(a), 3(d), 3(g), and 3(j)], corresponding to $\mu = 0.2\Lambda$

(small μ) and $\Omega R = 0, 10^{-3}, 5 \times 10^{-3}, 10^{-2}$ are quite similar to the plots from Fig. 2 corresponding to $\mu = 0$ and the same ΩR s. The onset of IMRC effect on destroying m is visible for larger values of $\Omega R = 5 \times 10^{-3}, 10^{-2}$. Comparing 2(c) with 3(g), and 2(d) with 3(j), it turns out that larger μ reinforces the formation of b [the slope of b in 3(g) and 3(j) are larger than the slope of b in 2(c)

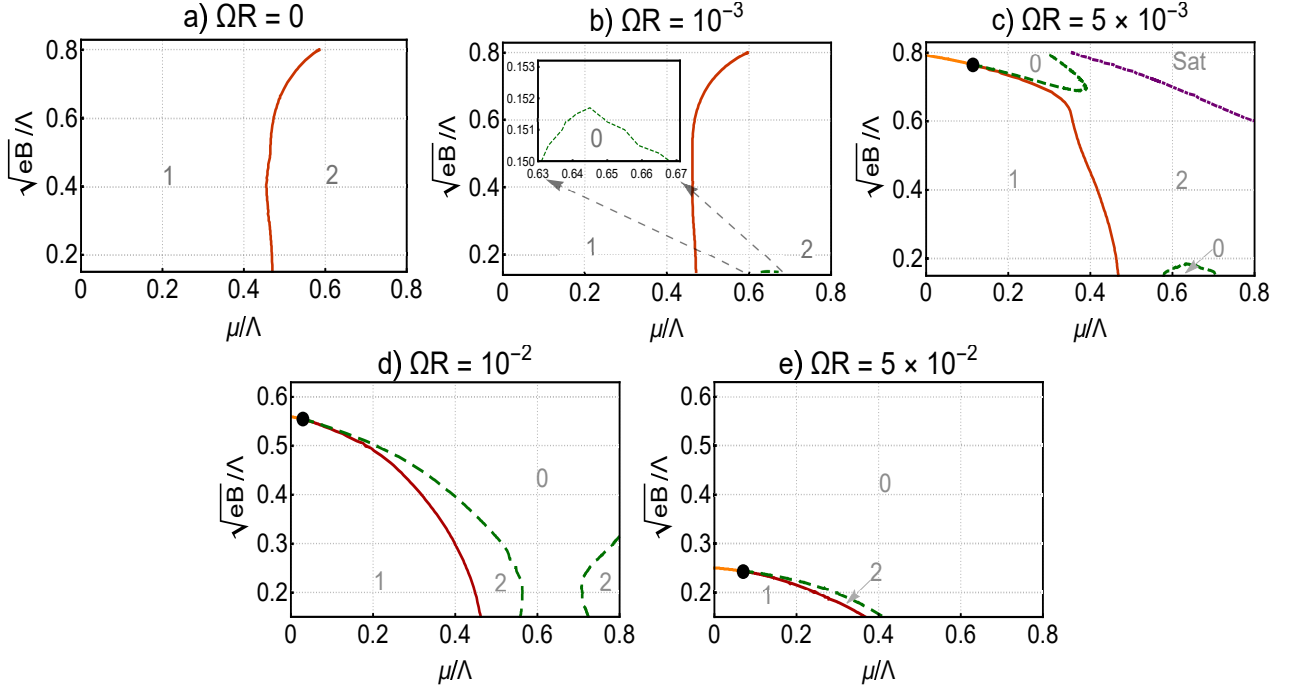


FIG. 5. color online. The phase portrait \sqrt{eB}/Λ vs. μ/Λ for fixed $\Omega R = 0, 10^{-3}, 5 \times 10^{-3}, 10^{-2}, 5 \times 10^{-2}$. The red solid lines separate two different regimes $\mu < m$ (denoted by "1") and $\mu > m$ (denoted by "2") in the MDCDW phase, and the orange solid and green dashed lines separate the MDCDW phase with $\mu < m$ and $\mu > m$ from the symmetry restored phase with $m = 0$ (denoted by "0"). Black circles demonstrate the position of the critical points at $(\mu, \sqrt{eB}) \sim (0.115\Lambda, 0.765\Lambda)$ (panel c), $(\mu, \sqrt{eB}) \sim (0.03\Lambda, 0.554\Lambda)$ (panel d) and $(\mu, \sqrt{eB}) \sim (0.069\Lambda, 0.243\Lambda)$ (panel e). The orange solid and green dashed lines correspond to first- and second-order phase transition lines, respectively. The regime denoted by "Sat", which is separated from the $\mu > m$ regime of the MDCDW phase by a dotted-dashed magenta line, shall be excluded from the phase diagram (see the description in text).

and 2(d)]. The critical value of eB , for which m and b vanish, is, however, smaller for nonvanishing μ .

For moderate values of $\mu = 0.4\Lambda$ and $\Omega R = 0, 10^{-3}$, the scenario is similar to the case of $\mu = 0.2\Lambda$ with the same ΩR 's [compare Figs. 3(b) and 3(e) with 3(a) and 3(d)]. For $\Omega R = 5 \times 10^{-3}$ and $\mu = 0.4\Lambda$, however, m decreases with increasing eB , whereas b increases rapidly with increasing eB [see Fig.3(h)]. The fact that m decreases for strong magnetic fields, moderate μ , and relatively large ΩR is related to the IMRC effect [25]. This effect becomes more apparent for larger values of $\Omega R = 0.01$, which is large enough to destroy m , and consequently b , in the regime $\sqrt{eB} \gtrsim 0.4\Lambda$ [see Fig. 3(k)].

This scenario completely changes for larger values of μ (see the plots in the third column of Fig. 3). Here, for $\mu = 0.6\Lambda$, b is larger than m , as long as $\Omega R \lesssim 0.005$ [see 3(c), 3(f), and 3(i)]. For large value of $\Omega R = 0.01$, both m and b vanish in the whole interval $\sqrt{eB} \in [0.15\Lambda, 0.8\Lambda]$ [see Fig. 3(l)]. This result coincides with the results presented in Figs. 1(j)-1(l). Comparing the plots from Figs. 3(j)-3(l), it turns out that for large $\Omega = 0.01$, the critical value of eB decreases with increasing μ . This is expected from the IMRC effect [25], and is completely visualized in these plots.

3. The ΩR dependence

In Fig. 4, the ΩR dependence of the chiral condensate m (solid orange) and spatial modulation b (dashed blue) is plotted for fixed values of μ and \sqrt{eB} . In each row μ is constant and \sqrt{eB} varies. In contrast, in each column \sqrt{eB} is constant and μ varies. The first to fourth rows correspond to $\mu = 0, 0.2\Lambda, 0.4\Lambda, 0.6\Lambda$, and the first to third columns correspond to $\sqrt{eB} = 0.15\Lambda, 0.25\Lambda$ and 0.45Λ . We notice that in contrast to previous figures, the ranges of the horizontal axes are not the same in all the plots from Fig. 4. Let us first compare the plots in each row: By comparing the plots from the first to third row [Figs. 4(a)-4(c), 4(d)-4(f), 4(g)-4(i)] together, it turns out that the interplay between the IMRC effect arising from a simultaneous increase of eB and ΩR leads to decreasing the critical value of ΩR with increasing eB . As concerns Figs. 4(j)-4(l) in the fourth row, however, large value of $\mu = 0.6\Lambda$ leads to $b > m$, in contrast to all the other plots. In Fig. 4(j), a remnant mass ($m \neq 0$) in the regime $\Omega R \lesssim 0.002$, similar to that which appeared in the third region of Fig. 1(a), leads to a relatively large b in this regime. By increasing \sqrt{eB} this remnant mass becomes larger, as expected from magnetic catalysis, and, at the same time, the critical ΩR decreases [compare Fig. 4(k) with 4(l)]. The latter can be regarded as a signature

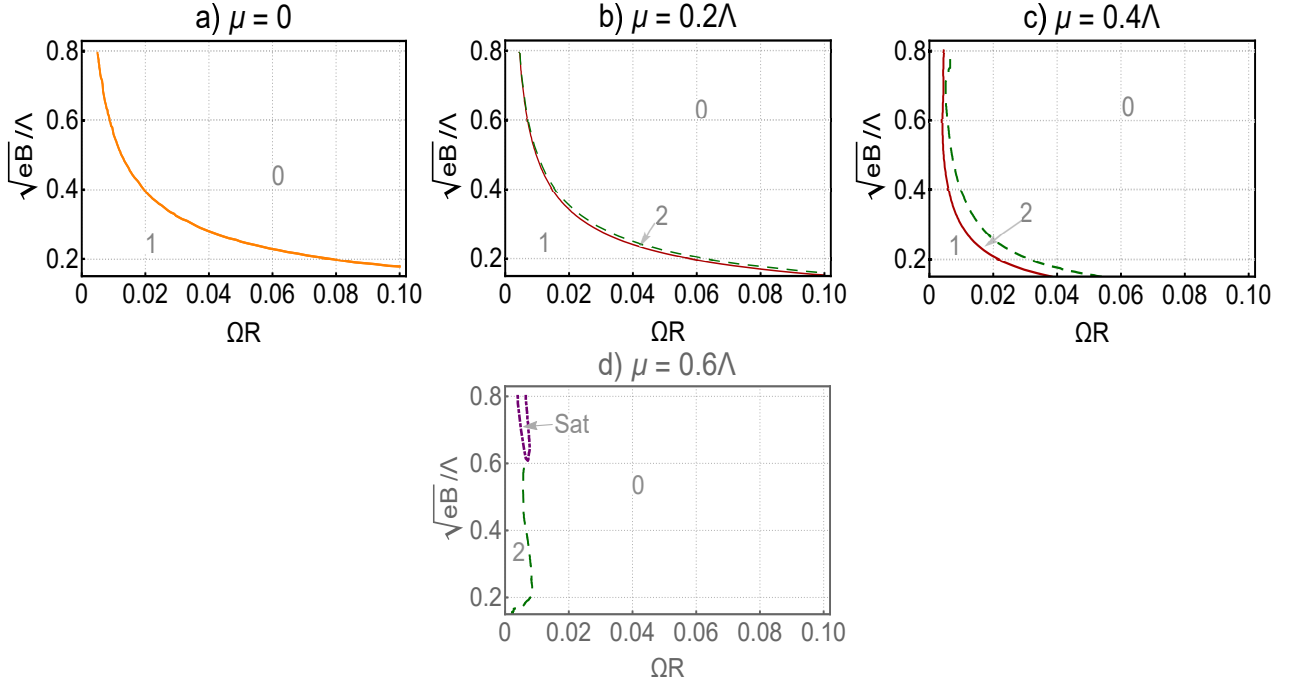


FIG. 6. color online. The phase portrait \sqrt{eB}/Λ vs. ΩR for fixed $\mu/\Lambda = 0, 0.2, 0.4, 0.6$. The red solid lines separate two different regimes $\mu < m$ (denoted by "1") and $\mu > m$ (denoted by "2") in the MDCDW phase, and the orange solid and green dashed lines separate the MDCDW phase with $\mu < m$ and $\mu > m$ from the symmetry restored phase with $m = 0$ (denoted by "0"). The orange solid line in panel (a) and the green dashed lines in panels (b)-(d) correspond to first- and second-order phase transitions. The regime denoted by "Sat", which is separated from the $\mu > m$ regime of the MDCDW phase by a dotted-dashed magenta line, shall be excluded from the phase diagram (see the description in text).

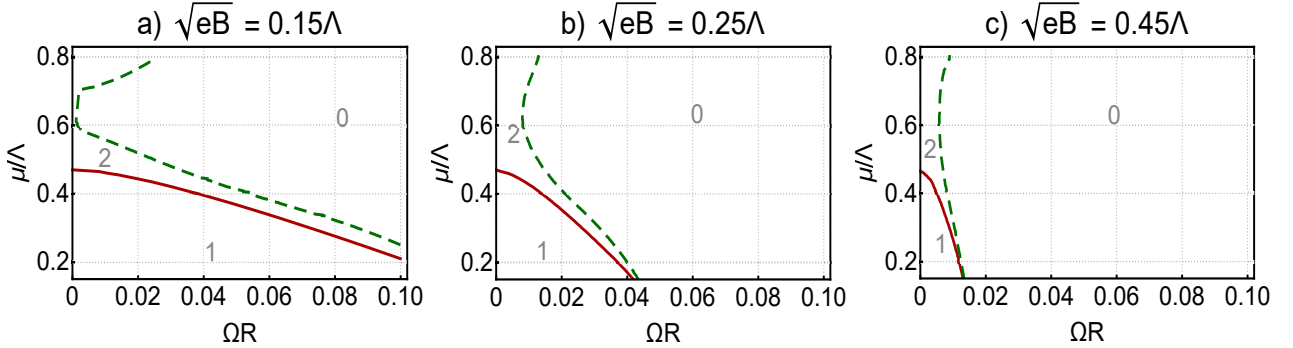


FIG. 7. color online. The phase portrait μ/Λ vs. ΩR for fixed $\sqrt{eB}/\Lambda = 0.15, 0.25, 0.45$. The red solid lines separate two different regimes $\mu < m$ (denoted by "1") and $\mu > m$ (denoted by "2") in the MDCDW phase, and the green dashed lines separate the MDCDW phase with $\mu > m$ from the symmetry restored phase with $m = 0$ (denoted by "0"). Green dashed lines correspond to second-order phase transition lines.

of IMRC effect.

B. Phase portraits $eB-\mu$, $eB-\Omega R$, and $\mu-\Omega R$

In this section, we present the phase portraits $\sqrt{eB}-\mu$ for fixed ΩR , $\sqrt{eB}-\Omega R$ for fixed μ , and $\mu-\Omega R$ for fixed \sqrt{eB} , and demonstrate the impact of the IMRC effect on the phase diagrams of this model, as well as similarities/differences between μ and ΩR in creating the MDCDW phase.

In Fig. 5, the phase portrait $\sqrt{eB}/\Lambda-\mu/\Lambda$ for fixed $\Omega R = 0, 10^{-3}, 5 \times 10^{-3}, 10^{-2}, 5 \times 10^{-2}$ is plotted. The red solid lines separate two different regimes $\mu < m$ (denoted by "1") and $\mu > m$ (denoted by "2") in the MDCDW phase, orange solid and green dashed lines separate the MDCDW phase with $\mu < m$ and $\mu > m$ from the symmetry restored phase with $m = 0$ (this normal phase is denoted by "0"). They correspond to first- and second-order phase transition lines, respectively. Figure 5(a) is comparable with the results presented in [18], where only two regimes $\mu < m$ and $\mu > m$ appear in the whole pa-

parameter space. For $\Omega R = 10^{-3}$, the parameter space is slightly different: A very small region of the normal phase appears in the interval $\mu \in [\sim 0.63\Lambda, \sim 0.67\Lambda]$ for small $\sqrt{eB} \lesssim 0.152\Lambda$ [see the sub-figure inserted into Fig. 5(b)]. The phase transition from the $\mu > m$ regime of the MDCDW phase to the normal phase is of second-order. This symmetry restored phase corresponds to the third region, which is demonstrated in Fig. 1(d). The $\sqrt{eB}/\Lambda - \mu/\Lambda$ phase diagram for $\Omega R = 0.005$ in Fig. 5(c) becomes more complex. Apart from two regimes $\mu < m$ and $\mu > m$ that are indicated by the red solid line, and the orange solid and green dashed lines that separate the MDCDW phase with $\mu < m$ and $\mu > m$ from the normal phase, there is another region in the upper right corner of the phase portrait which is separated by a magenta dotted-dashed line from the $\mu > m$ regime of the MDCDW phase. In this region, b is larger than $\Lambda = 1$ GeV, the cutoff of the model. This regime shall thus be completely excluded from the phase portrait. The black circle at $(\mu, \sqrt{eB}) \sim (0.115\Lambda, 0.795\Lambda)$ demonstrates the position of a critical point at the end of a second-order transition line.⁴

In Fig. 5(d) for $\Omega R = 0.01$, the phase portrait includes two regimes $\mu < m$ and $\mu > m$ in the MD-CDW phase. Because of the small $\mu > m$ regime in the lower right corner of the phase portrait, for $\sqrt{eB} \lesssim 0.3\Lambda$, a reentrance from the normal phase into the MD-CDW phase occurs for $\mu \gtrsim 0.75\Lambda$. For larger values of ΩR s, the normal phase becomes larger and the MD-CDW phase becomes suppressed. As it is demonstrated in Fig. 5(e), for $\Omega R = 0.05$ the MDCDW phase remains only in the left corner of the parameter space, in the interval $\mu \lesssim 0.4\Lambda$ and $\sqrt{eB} \lesssim 0.25\Lambda$. In both cases, the critical eB decreases with increasing μ . All these effects are the manifestation of the IMRC effect induced by an interplay between ΩR and eB . Apart from this aspect, a comparison between Figs. 5(d) and 5(e), the $\mu > m$ regime in the MDCDW phase becomes also very narrow (see the region between the solid red and dashed green lines in these figures), and a critical point appears in $(\mu, \sqrt{eB}) \sim (0.03\Lambda, 0.534\Lambda)$ for $\Omega R = 0.01$ in Fig. 5(d), which is then shifted to $(\mu, \sqrt{eB}) \sim (0.069\Lambda, 0.243\Lambda)$ in Fig. 5(e) for $\Omega R = 0.05$. Black circles in Figs. 5(d) and 5(e) demonstrate the position of these critical points.

In Fig. 6, the phase portrait $\sqrt{eB}/\Lambda - \Omega R$ for fixed $\mu/\Lambda = 0, 0.2, 0.4, 0.6$ is plotted. In Fig. 6(a), for $\mu = 0$ only the $m > \mu$ regime of the MDCDW phase appears in the left corner of the parameter space. As it is shown, the critical value of eB decreases with increasing ΩR . This is an indication of the IMRC effect. The transition from the $\mu < m$ regime of the MDCDW phase to the normal phase is of the first order. This confirms the results from Fig. 2, where, in particular, a first order phase transition

occurs for $\Omega R \gtrsim 0.005$ in Figs. 2(c)-2(e).

By increasing μ , an extremely narrow region with $\mu > m$ appears in the phase diagram. The red solid line in Fig. 6(b) separates two different regimes $\mu < m$ and $\mu > m$ in the MDCDW phase, and the green dashed line separates the MDCDW phase with $\mu > m$ from the normal phase. In Fig. 6(c), by increasing μ to $\mu = 0.4\Lambda$, the MDCDW phase becomes further suppressed, so that it completely disappears for $\Omega R \gtrsim 0.06$. For $\mu = 0.6\Lambda$, the $\mu < m$ regime of MDCDW phase completely disappears from the parameter space, and its $\mu > m$ regime is shifted to the left corner, where the critical eB does not significantly changes in terms of ΩR [see Fig. 6(d)]. This shows the interplay between eB , ΩR and μ in destroying the MDCDW phase through the IMRC effect

Finally, in Fig. 7, the phase portrait $\mu/\Lambda - \Omega R$ for fixed $\sqrt{eB}/\Lambda = 0.15, 0.25, 0.45$ is plotted. The red solid lines separate two different regimes $\mu < m$ (denoted by "1") and $\mu > m$ (denoted by "2") in the MDCDW phase, and the green dashed lines separate the MDCDW phase with $\mu > m$ from the normal phase (denoted by "0"). As it is shown in Fig. 7(a), for small values of $\sqrt{eB} = 0.25\Lambda$, the MDCDW phase exists even for large values of $\Omega R \sim 0.1$. The critical μ decreases with increasing ΩR [green dashed line in Fig. 7(a)]. For larger values of $\sqrt{eB} = 0.45\Lambda$, the MDCDW phase is completely shifted to the left corner of the parameter space. The $\mu > m$ regime in this phase is very narrow. A transition to the normal phase is only possible through this regime. The critical μ does not depend significantly on ΩR . Let us remind that all green dashed lines correspond to the second-order phase transitions.

V. CONCLUDING REMARKS

Starting with the Lagrangian density of a two-flavor gauged NJL model, and assuming a rigid rotation about a certain axis with a constant angular velocity Ω and a magnetic field eB aligned in the same direction, we defined two inhomogeneous condensates in order to introduce the MDCDW phase in a rotating, dense, and magnetized cold quark matter. The question was whether this phase survives the extreme conditions prevailing, e.g., in a neutron star. In contrast to [22], the temperature and its possible interplay with high densities, constant magnetic fields and angular velocities does not play any role in the present paper. We consider a low temperature limit and showed that the temperature dependent thermodynamic potential vanishes in this limit. Taking this limit is justified by the assumption that the neutron star rotates with a constant angular velocity [23].

We first determined the energy eigenvalues of the model, and showed that in comparison with the nonrotating case, they are shifted by a term Ωj , where $j = \ell + 1/2$ is the corresponding quantum number to $J_z = L_z + \Sigma_z/2$ (see Sec. II for more details). We then determined in Sec. III, the corresponding thermodynamic potential to

⁴ The point is not a tricritical point because, according to the above description, the two regimes $\mu < m$ and $\mu > m$ are two distinct "regimes" in one and the same chirally broken MD-CDW phase.

this model at finite temperature T , chemical potential μ , and magnetic field eB . We showed that it consists of three parts, a vacuum part $V_{T=0}$, an μ, Ω dependent part $V_{\mu, \Omega}$, and a temperature dependent part $V_{T \neq 0}$ [see (III.12)]. The latter vanishes by taking the limit $T \rightarrow 0$. We thus focused on $V_{T=0}$ and $V_{\mu, \Omega}$. As it is argued, $V_{T=0}$ is independent of Ω . To regularize it, we used the same proper-time regularization scheme as in [18, 22]. This gives us the possibility to compare our numerical results for $\Omega = 0$ with the results presented in these two papers. The final expression for $V_{T=0}$ is given in (III.16), where a summation over Landau levels is already performed. As concerns $V_{\mu, \Omega}$ from (III.17), we first separated it into two parts: The LLL and HLL parts, that are given in (III.18) and (III.19). To derive the LLL part, we followed step by step the same regularization method as is described in the Appendix of [18]. We showed, in particular, that the LLL part of the potential includes an anomalous term proportional to $b\Omega$, apart from a term proportional to $b\mu$, which appears originally in [18] (see (III.24)). This term appears as a consequence of the asymmetry appearing in the energy dispersion relations of the lowest and higher Landau levels and, according to [12], leads to important topological effects (see below for further discussions). Another difference comparing to the nonrotating case from [18], appears in the HLL part of the effective potential, whose final result which is given in (III.32) depends explicitly on Ω .

Minimizing the thermodynamic potential with respect to two dynamical variables m and b , the chiral and spatial modulation condensates, we studied in Sec. IV, the μ, eB , and ΩR dependence of these two gaps, separately. We showed, that at $\mu = 0$, nonvanishing ΩR acts as an additional chemical potential.⁵ For small ΩR up to $\Omega R \sim 0.005$, the rotation enhances the production of b and thus the MDCDW phase, even for vanishing μ . Once ΩR and eB become larger, b vanishes because of the IMRC effect and the resulting suppression of m (see Fig. 2). For nonvanishing μ , the situation is worse. Here, the IMRC effect is amplified because of the similar roles played by ΩR and μ . They act as inverse magnetic catalyzers (magnetic inhibitors). According to the results from Fig. 4, we conclude that, because of the IMRC effect, the MDCDW phase is suppressed in the regimes of eB, μ , and ΩR that are relevant for cold neutron stars.

In the second part of Sec. IV, we further explored the eB - μ , eB - ΩR , and μ - ΩR phase portraits. We showed that, as expected from [18], the MDCDW phase consists of two regimes: $\mu < m$ and $\mu > m$. The transition from the first regime $\mu < m$ to the normal (chiral symmetry restored) phase is of the first order, whereas the transition from the second regime $\mu > m$ to the normal phase is of the second-order. The results from this part confirm the conclusion concerning the role of IMRC effect on destroying the MDCDW phase in regimes that are relevant

for the cold neutron stars. The fact that the critical magnetic field decreases with increasing ΩR (μ) for fixed μ (ΩR) is a direct consequence of the IMRC effect.

Because of the aforementioned similarity between μ and ΩR , the MDCDW phase is created even at $\mu = 0$ for $\Omega R > 0$. This is in particular demonstrated in the plots of Fig. 2 and the phase portrait in Fig. 6(a). According to these results, the critical value of eB decreases with increasing ΩR for $\mu \leq 0.4\Lambda$. This opens the possibility for the MDCDW phase to be created during the early stages of heavy ion collisions, where $\mu \sim 0$, $\sqrt{eB} \sim 0.1 - 0.5$ GeV ($eB \sim 5 - 15 m_\pi^2$ with the pion mass $m_\pi \sim 140$ MeV) [32], and $\Omega R \sim 0.1$ [33]. Here, however, it is necessary to consider the effect of finite temperature and its interplay with the magnetic field and rotation. First results in this direction is recently presented in [34], where the effect of magnetic fields is neglected. In [35], the effects of rotation on confining properties of compact electrodynamics in two spatial dimensions is studied. It is, in particular, shown that at finite temperature the phase diagram of a uniformly rotating system possesses, in addition to a confining phase at low temperature and a deconfining phase at high temperature, a mixed inhomogeneous phase at intermediate temperatures. The latter has a confining region at the core and a deconfining region at the edge of the rotating system. It would be interesting to extend the present work in this direction.

As aforementioned, in this paper, we focused on the MDCDW phase in rotating cold quark matter. This phase is characterized by a certain asymmetry in its LLL spectrum. As it is shown in [19], this asymmetry which occurs also in the nonrotating case, arises by the interplay between the inhomogeneous condensate and the magnetic field. It is also shown to be the origin of the nontrivial topological properties of this model, leading, in particular, to the creation of an anomalous, nondissipative electric Hall current in the corresponding Maxwell equations. As it is argued in [19], in the nonrotating case, the anomalous baryon (quark) number density ρ_{an}^B associated with this anomalous four-current is related to the regularized Atiyah-Parodi-Singer (APS) index η_B [36] via

$$\eta_B \equiv \lim_{s \rightarrow 0} \sum_k \text{sgn}(E_k) |E_k|^{-s} = -2 \int d^3x \rho_{\text{an}}^B,$$

with

$$\rho_{\text{an}}^B \equiv \sum_f \frac{N_c b |q_f eB|}{2\pi^2}. \quad (\text{V.1})$$

Here, b is the spatial modulation in the MDCDW phase and N_c the number of colors. According to [19], another way to determine ρ_{an}^B is by appropriately regularizing the anomalous part of the thermodynamic potential corresponding to the MDCDW phase in a nonrotating phase [18]. According to [18],

$$\mathcal{V}_{\text{anomal}} \Big|_{\Omega=0} = -\rho_{\text{an}}^B \mu,$$

with baryonic charge density given in (V.1). As concerns the rotating case, we determined in Sec. III, the

⁵ The fact that ΩN , with $N = j_{\text{max}}$, is an ‘‘effective’’ chemical potential, is also indicated in [24].

anomalous part of the thermodynamic potential of the MDCDW model in a rotating medium. It is given in (III.24) and leads to

$$\mathcal{V}_{\text{anomal}}|_{\Omega \neq 0} = -(\rho_{\text{an}}^B \mu + \rho_{\text{an}}^\Omega \Omega),$$

where ρ_{an}^B is given in (V.1), and ρ_{an}^Ω reads

$$\rho_{\text{an}}^\Omega = \sum_f \text{sgn}(q_f) \frac{N_c b |q_f e B|}{8\pi^2} \frac{R^2}{L_{f,B}^2}, \quad (\text{V.2})$$

with R the radius of the rotating cylinder and the magnetic length $L_{f,B} \equiv |q_f e B|^{-1/2}$. Let us notice that ρ_{an}^Ω arises from the summation over a flavor dependent ℓ in (III.22) [for the limits of ℓ , see (III.5)], where Ωj played the role of a chemical potential associated with rotation [24]. In analogy to ρ_{an}^B , ρ_{an}^Ω from (V.2) leads immediately to anomalous electric charge density $J_\Omega^0 \equiv \sum_f e q_f \rho_{\text{an},f}^\Omega$ associated to $\rho_{\text{an},f}^\Omega$ for each flavor, which may appear in the corresponding Maxwell equation as its baryonic counterpart $J_B^0 \equiv \sum_f e q_f \rho_{\text{an},f}^B$ in [19]. It would be interesting to find the relation between ρ_{an}^Ω and the APS index η via an appropriate regularization of $\eta \equiv \lim_{s \rightarrow 0} \sum_k \text{sgn}(E_k) |E_k|^{-s}$ in the presence of Ω . We postpone this computation to our future works.

ACKNOWLEDGEMENTS

The authors thank M. H. Gholami for his collaboration in the early stages of this work. We also thank M. Sh. Sadeghi and Sh. Baghran for valuable discussions.

Appendix A: The spectrum of the model

In this appendix, we solve the eigenvalue equation $\mathcal{H}_f \psi_f = E_f \psi_f$ from (II.11) in an appropriate cylindrical coordinate system, described by $x^\mu = (t, x, y, z) = (t, \rho \cos \varphi, \rho \sin \varphi, z)$, where ρ is the radial coordinate, φ the azimuthal angle, and z the height.

$$\mathcal{D}_f^\pm = \begin{pmatrix} \mp p_z + b s_f & \pm i e^{-i\varphi} (\partial_\rho - \frac{i}{\rho} \partial_\varphi) \mp i \frac{q_f e B}{2} \rho e^{-i\phi} \\ \pm i e^{i\varphi} (\partial_\rho + \frac{i}{\rho} \partial_\varphi) \pm i \frac{q_f e B}{2} \rho e^{i\phi} & \pm p_z - b s_f \end{pmatrix}. \quad (\text{A.7})$$

From (A.5), we obtain

$$[(\mathcal{H}_f + \Omega J_z)^2 - m^2] \psi_f = \mathcal{N}_f \psi_f, \quad (\text{A.8})$$

with

$$\mathcal{N}_f \equiv \begin{pmatrix} \mathcal{E}_f^{--} & 0 & 2m b s_f & 0 \\ 0 & \mathcal{E}_f^{+-} & 0 & -2m b s_f \\ 2m b s_f & 0 & \mathcal{E}_f^{-+} & 0 \\ 0 & -2m b s_f & 0 & \mathcal{E}_f^{++} \end{pmatrix}, \quad (\text{A.9})$$

To do this, let us first consider \mathcal{H}_f from (II.12),

$$\mathcal{H}_f = \begin{pmatrix} \mathcal{O} + b s_f \tau_3 - \Omega J_z & m \\ m & -\mathcal{O} + b s_f \tau_3 - \Omega J_z \end{pmatrix}, \quad (\text{A.1})$$

with \mathcal{O} given by

$$\mathcal{O} \equiv \tau_1 (i \partial_x - q_f e B y / 2) + \tau_2 (i \partial_y + q_f e B x / 2) + i \tau_3 \partial_z. \quad (\text{A.2})$$

Using the representation of the total angular momentum in the cylindrical coordinate system $J_z = L_z + \Sigma_z / 2 = -i \partial_\varphi + \Sigma_z / 2$, with $\Sigma_z = \mathbb{I}_{2 \times 2} \otimes \tau_3$, it is easy to check that \mathcal{H}_f commutes with J_z . They thus have simultaneous eigenfunctions. The latter has the general form

$$\psi_f(\rho, \varphi, z) = e^{i p_z z} \begin{pmatrix} e^{i\ell - \varphi} f_1(\rho) \\ e^{i\ell + \varphi} f_2(\rho) \\ e^{i\ell - \varphi} f_3(\rho) \\ e^{i\ell + \varphi} f_4(\rho) \end{pmatrix}, \quad (\text{A.3})$$

and satisfies the eigenvalue equation for the total angular momentum,

$$J_z \psi_f(\rho, \varphi, z) = j \psi_f(\rho, \varphi, z). \quad (\text{A.4})$$

Here, $\ell_\pm \equiv j \pm 1/2$. To determine $f_i(\rho)$, $i = 1, \dots, 4$, let us consider the energy eigenfunction equation (II.11), with \mathcal{H}_f given in (A.1). Plugging $\psi_f(\rho, \varphi, z)$ from (A.3) into this relation we arrive first at

$$(\mathcal{H}_f + \Omega J_z) \psi_f = \mathcal{M}_f \psi_f, \quad (\text{A.5})$$

with \mathcal{M}_f given by

$$\mathcal{M}_f \equiv \begin{pmatrix} \mathcal{D}_f^+ & m \\ m & \mathcal{D}_f^- \end{pmatrix}, \quad (\text{A.6})$$

and

and

$$\begin{aligned} \mathcal{E}_f^{\mp\mp} &\equiv -\partial_\rho^2 - \frac{1}{\rho} \partial_\rho - \frac{1}{\rho^2} \partial_\phi^2 + i q_f e B \partial_\phi \mp q_f e B \\ &\quad + \left(\frac{q_f e B \rho}{2} \right)^2 + (p_z \mp s_f b)^2, \\ \mathcal{E}_f^{\pm\mp} &\equiv -\partial_\rho^2 - \frac{1}{\rho} \partial_\rho - \frac{1}{\rho^2} \partial_\phi^2 + i q_f e B \partial_\phi \pm q_f e B \\ &\quad + \left(\frac{q_f e B \rho}{2} \right)^2 + (p_z \mp s_f b)^2. \end{aligned} \quad (\text{A.10})$$

As it turns out, the above matrix \mathcal{N}_f commutes with the diagonal matrix

$$\widetilde{\mathcal{N}}_f \equiv \begin{pmatrix} \widetilde{\mathcal{E}}_f^- & 0 & 0 & 0 \\ 0 & \widetilde{\mathcal{E}}_f^+ & 0 & 0 \\ 0 & 0 & \widetilde{\mathcal{E}}_f^- & 0 \\ 0 & 0 & 0 & \widetilde{\mathcal{E}}_f^+ \end{pmatrix}, \quad (\text{A.11})$$

with

$$\begin{aligned} \widetilde{\mathcal{E}}_f^\mp &= -\partial_\rho^2 - \frac{1}{\rho}\partial_\rho - \frac{1}{\rho^2}\partial_\varphi^2 + iq_f eB \partial_\varphi \mp q_f eB \\ &+ \left(\frac{q_f eB \rho}{2} \right)^2. \end{aligned} \quad (\text{A.12})$$

This help us to determine the eigenfunction ψ_f in (A.8). Hence, the problem is reduced to determining the eigenfunction ψ_f and the eigenvalue λ_f in

$$\widetilde{\mathcal{N}}_f \psi_f = \lambda_f \psi_f. \quad (\text{A.13})$$

Applying $\widetilde{\mathcal{N}}_f$ from (A.11) to ψ_f from (A.3), we arrive at two differential equations for $f_i(\rho), i = 1, \dots, 4$,

$$\begin{aligned} \left[\partial_\rho^2 + \frac{1}{\rho}\partial_\rho - \frac{\ell_\mp^2}{\rho^2} + q_f eB (\ell_\mp \pm 1) - \left(\frac{q_f eB \rho}{2} \right)^2 \right. \\ \left. + \lambda_f \right] f_\mp(\rho) = 0, \end{aligned} \quad (\text{A.14})$$

where $f_- \equiv f_1 = f_3$ and $f_+ \equiv f_2 = f_4$ are introduced. To solve these equations, we use the ansatz

$$f_\mp(x) = e^{-\frac{x}{2}} x^{|\ell_\mp|/2} g_\mp(x), \quad (\text{A.15})$$

with $x \equiv |q_f eB| \rho^2/2$. Plugging (A.15) into (A.14), the resulting equation reads

$$\left[x \partial_x^2 + (|\ell_\mp| + 1 - x) \partial_x + \kappa_\mp \right] g_\mp(x) = 0, \quad (\text{A.16})$$

where

$$\kappa_\mp \equiv \frac{\lambda_f}{2|q_f eB|} + \frac{s_f (\ell_\mp \pm 1) - |\ell_\mp| - 1}{2}. \quad (\text{A.17})$$

The differential equation (A.16) is comparable with the Kummer's differential equation

$$(z \partial_z^2 + (b - z) \partial_z - a) g(z) = 0, \quad (\text{A.18})$$

whose solution

$$g(z) = A_1 F_1(a; b; z) + B U(a; b; z), \quad (\text{A.19})$$

is a linear combination of a hypergeometric function of the first and second kind ${}_1F_1(a; b; z)$ and $U(a; b; z)$.⁶ Requiring that $g_\mp(x)$ are regular at $x \rightarrow 0$, $g_\mp(x)$ is given by

$$g_\mp(x) = A_{\mp 1} F_1(-\kappa_\mp; |\ell_\mp| + 1, x). \quad (\text{A.20})$$

⁶ Similar results are also found in [24, 25, 30].

Plugging this result into (A.15), we thus arrive at

$$f_\mp(x) = A_\mp e^{-\frac{x}{2}} x^{|\ell_\mp|/2} {}_1F_1(-\kappa_\mp; |\ell_\mp| + 1, x). \quad (\text{A.21})$$

Assuming, at this stage, that the fermionic system has no spatial boundary condition, the hypergeometric function can be replaced by the associated Laguerre polynomial,

$${}_1F_1(-\kappa_\mp; |\ell_\mp| + 1, x) = \frac{|\ell_\mp|! \kappa_\mp!}{(|\ell_\mp| + \kappa_\mp)!} L_{\kappa_\mp}^{|\ell_\mp|}(x). \quad (\text{A.22})$$

Moreover, introducing $n \equiv \frac{\lambda_f}{2|q_f eB|}$ in (A.17), it turns out that in this case $n \in \mathbb{N}_0$. Using the orthonormality relation of the Laguerre polynomial

$$\int_0^\infty dz z^\alpha L_n^\alpha(z) L_m^\alpha(z) = \frac{(n + \alpha)!}{n!} \delta_{m,n}, \quad (\text{A.23})$$

we arrive at

$$f_\mp(x) = \left(\frac{|q_f eB|}{2\pi} \frac{\kappa_\mp}{(\kappa_\mp + |\ell_\mp|)!} \right)^{1/2} e^{-\frac{x}{2}} x^{|\ell_\mp|/2} L_{\kappa_\mp}^{|\ell_\mp|}(x). \quad (\text{A.24})$$

Plugging this result into (A.3), the eigenfunction ψ_f in (II.11) reads

$$\psi_f(\rho, \varphi, z) = e^{ip_z z} \begin{pmatrix} e^{i\ell_- \varphi} f_-(x) \\ e^{i\ell_+ \varphi} f_+(x) \\ e^{i\ell_- \varphi} f_-(x) \\ e^{i\ell_+ \varphi} f_+(x) \end{pmatrix}, \quad (\text{A.25})$$

with $x = |q_f eB| \rho^2/2$ and f_\mp from (A.24). At this stage, we shall determine κ_\mp . To do this, we use the fact that the lower index κ_\pm in the Laguerre polynomial shall be positive. According to (A.17), depending on ℓ , this leads for the two cases of positive and negative q_f , or alternatively positive and negative s_f , to different allowed values for κ_\mp . The results for $\ell \leq -1$ and $\ell \geq 0$ are summarized in Tables I and II (see also [25] for more details).

TABLE I. The allowed values for $\kappa_s, s \equiv \pm$ for $\ell \leq -1, \ell \geq 0$, and positive and negative charges, according to (A.17).

	$\ell \leq -1$	$\ell \geq 0$
$s_f = +1, s = -1$	$\kappa_- = n + \ell$	$\kappa_- = n$
$s_f = +1, s = +1$	$\kappa_+ = n + \ell$	$\kappa_+ = n - 1$
$s_f = -1, s = -1$	$\kappa_- = n - 1$	$\kappa_- = n - \ell - 1$
$s_f = -1, s = +1$	$\kappa_+ = n$	$\kappa_+ = n - \ell - 1$

According to the results from Table II, the energy eigenfunctions for $n = 0$ are different from the ones for $n \neq 0$: For $n = 0$ and $s_f = +1$ (positive charges), we have

$$\psi_f^{n=0, s_f=+1} = e^{ip_z z} e^{i\ell_- \varphi} f_-(x) \begin{pmatrix} 1 \\ 0 \\ 1 \\ 0 \end{pmatrix}, \quad (\text{A.26})$$

TABLE II. The allowed values for $n = \frac{\lambda_f}{2|q_f e B|}$ for $s = \mp 1$, corresponding to κ_{\mp} , and positive and negative charges, according to Table I. To determine these ranges, we set $\kappa_{\mp} \geq 0$ in Table I.

$s_f = +1, s = -1$	$n = 0$	$\ell = 0, 1, 2, \dots$
	$n \geq 1$	$\ell = -n, -n + 1, \dots, -2, -1, 0, 1, 2, \dots$
$s_f = +1, s = +1$	$n = 0$	—
	$n \geq 1$	$\ell = -n, -n + 1, \dots, -2, -1, 0, 1, 2, \dots$
$s_f = -1, s = -1$	$n = 0$	—
	$n \geq 1$	$\ell = \dots, -2, -1, 0, 1, 2, \dots, n - 2, n - 1$
$s_f = -1, s = +1$	$n = 0$	$\ell = \dots, -2, -1$
	$n \geq 1$	$\ell = \dots, -2, -1, 0, 1, 2, \dots, n - 2, n - 1$

whereas for $s_f = -1$ (negative charges), we obtain

$$\psi_f^{n=0, s_f=-1} = e^{ip_z z} e^{i\ell + \varphi} f_{+}(x) \begin{pmatrix} 0 \\ 1 \\ 0 \\ 1 \end{pmatrix}. \quad (\text{A.27})$$

For $n \geq 1$, the eigenfunctions are given by (A.25).

To determine the energy eigenvalues E_f , we have to distinguish between $n = 0$ and $n \neq 0$ for positive ($s_f = +1$) and negative ($s_f = -1$) charges. For $n = 0$ and $s_f = +1$ as well as $s_f = -1$, we plug (A.26) as well as (A.27) into (A.5) and use (II.11) to arrive at

$$\begin{pmatrix} \mp p_z + b & m \\ m & \pm p_z + b \end{pmatrix} \psi_f^{n=0, s_f=\pm 1} = (E_f + \Omega j) \psi_f^{n=0, s_f=\pm 1}. \quad (\text{A.28})$$

Here, we have reduced the 4×4 matrix equation to a 2×2 one. This leads to the energy dispersion relation

$$E_f^{n=0} = -\Omega j + b + \epsilon \sqrt{p_z^2 + m^2}, \quad (\text{A.29})$$

for $n = 0$ (see (II.13)). For $n > 0$, we plug (A.25) into (A.8) and combine the result with (A.13) and (II.11) to arrive first at

$$\begin{pmatrix} \mathcal{K}_{-s_f} & 0 & +2ms_f b & 0 \\ 0 & \mathcal{K}_{+s_f} & 0 & -2ms_f b \\ +2ms_f b & 0 & \mathcal{K}_{-s_f} & 0 \\ 0 & -2ms_f b & 0 & \mathcal{K}_{+s_f} \end{pmatrix} \psi_f = 0, \quad (\text{A.30})$$

with

$$\mathcal{K}_{\mp} \equiv 2n|q_f e B| + (p_z \mp s_f b)^2 - [(E_f + \Omega j)^2 - m^2]. \quad (\text{A.31})$$

This leads to the energy dispersion relation

$$E_f^{n>0} = -\Omega j + \zeta \left[\left(b + \epsilon \sqrt{p_z^2 + m^2} \right)^2 + 2n|q_f e B| \right]^{1/2}, \quad (\text{A.32})$$

for $n > 0$ (see (II.14)).

Appendix B: Supplementary results

1. The p_z integration in (III.20)

Let us consider the integration over p_z , which appears in $\mathcal{V}_{\mu, \Omega}^{n=0}$ from (III.20),

$$\mathcal{V}_{f, \ell} = \sum_{\epsilon=\pm 1} \int_{-\infty}^{\infty} dp_z \left(|E_f^{n=0} - \mu| - |E_f^{n=0, \Omega=0}| \right). \quad (\text{B.1})$$

Using the definition of $E_f^{n=0}$, and performing the summation over ϵ , we first arrive at

$$\mathcal{V}_{f, \ell} = 2 (J^{\text{mom}}(a_1) - J^{\text{mom}}(a_2)), \quad (\text{B.2})$$

with

$$J^{\text{mom}}(a) \equiv \int_0^{\Lambda} dp_z (|a + \omega(p_z)| + |a - \omega(p_z)|), \quad (\text{B.3})$$

and $a_1 \equiv b - \Omega j - \mu$ and $a_2 \equiv b$. In (B.3), $\omega(p)$ is defined by $\omega(p) \equiv \sqrt{p^2 + m^2}$. Using

$$\begin{aligned} \int_0^{\Lambda} dp_z |a + \omega(p_z)| &= \begin{cases} I(0, \Lambda) + a\Lambda, & a > -|m|, \\ -I(0, P_a) + I(P_a, \Lambda) - 2aP_a + a\Lambda, & a < -|m|, \end{cases} \\ \int_0^{\Lambda} dp_z |a - \omega(p_z)| &= \begin{cases} -I(0, P_a) + I(P_a, \Lambda) + 2aP_a - a\Lambda, & a > |m|, \\ I(0, \Lambda) - a\Lambda, & a < |m|, \end{cases} \end{aligned} \quad (\text{B.4})$$

with $P_a \equiv \sqrt{a^2 - m^2}$, and

$$I(\Lambda_1, \Lambda_2) \equiv \int_{\Lambda_1}^{\Lambda_2} dp_z \omega(p_z) = \frac{1}{2} \left[\Lambda_2 \omega(\Lambda_2) - \Lambda_1 \omega(\Lambda_1) + m^2 \ln \left(\frac{\Lambda_2 + \omega(\Lambda_2)}{\Lambda_1 + \omega(\Lambda_1)} \right) \right], \quad (\text{B.5})$$

we arrive at [18]

$$J^{\text{mom}}(a) = \begin{cases} 2I(P_a, \Lambda) + 2aP_a, & |m| < a, \\ 2I(0, \Lambda), & -|m| < a < |m|, \\ 2I(P_a, \Lambda) - 2aP_a, & a < -|m|. \end{cases} \quad (\text{B.6})$$

Plugging (B.6) into (B.2), we obtain (III.21).

2. The final expression for $\mathcal{K}_{f,\epsilon,n}(p_z)$ in (III.32)

In this section, we present the final expression for $\mathcal{K}_{f,\epsilon,n}(p_z)$ defined by

$$\mathcal{K}_{f,\epsilon,n}(p_z) \equiv \sum_{k=0}^{N_f-1} \mathcal{J}_{f,\epsilon,n,k}(p_z), \quad (\text{B.7})$$

where $\mathcal{J}_{f,\epsilon,n,k}(p_z)$ is defined in (III.30). We perform the summation over k in (B.7) using an appropriate Mathematica program and arrive at the following conditional expression:

$$\mathcal{K}_{f,\epsilon,n}(p_z) = \mathcal{A}_i \quad \text{if } \mathcal{C}_i, \quad \text{for } i = 1, \dots, 10, \quad (\text{B.8})$$

with

$$\begin{aligned} \mathcal{A}_1 &\equiv -\Omega E_+^+, \\ \mathcal{A}_2 &\equiv -\frac{1}{2} \Omega \mathcal{N}_f (2E_-^- - (\mathcal{N}_f - 1)), \\ \mathcal{A}_3 &\equiv -\frac{1}{2} \Omega \mathcal{N}_f (2E_+^+ + (\mathcal{N}_f - 1)), \\ \mathcal{A}_4 &\equiv -\frac{1}{2} \Omega ([E_-^-] - \mathcal{N}_f) ([E_-^-] - (2E_-^- + 1 - \mathcal{N}_f)), \\ \mathcal{A}_5 &\equiv -\frac{1}{2} \Omega (([E_-^-] - (2E_-^- + 1)) [E_-^-] + 2E_+^+ + \mathcal{N}_f (2E_-^- + 1 - \mathcal{N}_f)), \\ \mathcal{A}_6 &\equiv -\frac{1}{2} \Omega (2E_+^+ - [E_+^+]) ([-E_+^+] + 1), \\ \mathcal{A}_7 &\equiv -\frac{1}{2} \Omega (([E_-^-] - (2E_-^- + 1)) [E_-^-] + ([E_+^+] - (2E_+^+ + 1)) [E_+^+] + 2(E_+^+ + E_-^- \mathcal{N}_f) + \mathcal{N}_f (1 - \mathcal{N}_f)), \\ \mathcal{A}_8 &\equiv -\frac{1}{2} \Omega ([E_-^-] - [E_+^+] - 1) ([E_-^-] + [E_+^+] - 2E_-^-), \\ \mathcal{A}_9 &\equiv -\frac{1}{2} \Omega (([E_-^-] - (2E_-^- + 1)) [E_-^-] - ([E_+^+] - (2E_+^+ - 1)) [E_+^+] + 4E_+^0), \\ \mathcal{A}_{10} &\equiv -\frac{1}{2} \Omega (([E_-^-] - (2E_-^- + 1)) [E_-^-] + ([E_+^+] - (2E_+^+ + 1)) [E_+^+] - ([E_-^-] - (2E_-^- - 1)) [E_+^+] + 4E_+^0), \end{aligned} \quad (\text{B.9})$$

and the conditions

$$\begin{aligned}
\mathcal{C}_1 &\equiv E_+^+ = 0 \wedge \mu_f < 0 \wedge E_+^- > \mathcal{N}_f - 1 \wedge E_+ > 0 \wedge \mathcal{N}_f > 1 \wedge \Omega > 0, \\
\mathcal{C}_2 &\equiv E_+^- < 0 \wedge E_+ > 0 \wedge \mathcal{N}_f > 1 \wedge E_+^+ > 0 \wedge \Omega > 0, \\
\mathcal{C}_3 &\equiv \mu_f < 0 \wedge E_+^+ < 0 \wedge E_+^- > \mathcal{N}_f - 1 \wedge E_+ > 0 \wedge \mathcal{N}_f > 1 \wedge \Omega > 0 \wedge E_+^+ \leq 1 - \mathcal{N}_f, \\
\mathcal{C}_4 &\equiv E_+ > 0 \wedge \mathcal{N}_f > 1 \wedge E_+^- \geq 0 \wedge E_+^- < \mathcal{N}_f - 1 \wedge [E_+^+ > 0 \vee (E_+^+ = 0 \wedge \Omega \leq 0)], \\
\mathcal{C}_5 &\equiv E_+ > 0 \wedge \mu_f < 0 \wedge \mathcal{N}_f > 1 \wedge \Omega > 0 \wedge E_+^+ = 0 \wedge E_+^- < \mathcal{N}_f - 1, \\
\mathcal{C}_6 &\equiv \mu_f < 0 \wedge E_+^+ < 0 \wedge E_+^+ > 1 - \mathcal{N}_f \wedge E_+^- > \mathcal{N}_f - 1 \wedge E_+ > 0 \wedge \mathcal{N}_f > 1, \\
\mathcal{C}_7 &\equiv E_+ > 0 \wedge \mu_f < 0 \wedge \mathcal{N}_f > 1 \wedge E_+^+ < 0 \wedge E_+^- < \mathcal{N}_f - 1, \\
\mathcal{C}_8 &\equiv E_+^- = \mathcal{N}_f - 1 \wedge E_+ > 0 \wedge \mathcal{N}_f > 1 \wedge E_+ > \mu_f \\
&\quad \wedge ((\Omega \leq 0 \wedge (E_+ + \mu_f \geq 0 \vee \Omega[E_+^+ + (\mathcal{N}_f - 1)] \leq 0)) \vee E_+^+ > 0), \\
\mathcal{C}_9 &\equiv E_+ > 0 \wedge \mu_f < 0 \wedge \mathcal{N}_f > 1 \wedge \Omega > 0 \wedge E_+^+ = 0 \wedge E_+^- = \mathcal{N}_f - 1, \\
\mathcal{C}_{10} &\equiv \mathcal{N}_f > 1 \wedge E_+ > 0 \wedge \mu_f < 0 \wedge E_+^- = \mathcal{N}_f - 1 \wedge E_+^+ < 0 \wedge E_+^+ > 1 - \mathcal{N}_f.
\end{aligned} \tag{B.10}$$

In the above expressions, $E^{\pm,0}$ are defined by

$$E_+^{\pm} \equiv \frac{E_+ \pm \mu_f}{\Omega}, \quad E_+^0 \equiv \frac{E_+}{\Omega}. \tag{B.11}$$

Here, E_+ and μ_f for $f = \{u, d\}$ are defined in (III.26) and (III.31).

-
- [1] W. Busza, K. Rajagopal and W. van der Schee, *Heavy-ion collisions: The big picture, and the big questions*, Ann. Rev. Nucl. Part. Sci. **68**, 339 (2018), arXiv:1802.04801 [hep-ph].
- [2] A. Lovato, T. Dore, R. D. Pisarski, B. Schenke, K. Chatzioannou, J. S. Read, P. Landry, P. Danielewicz, D. Lee and S. Pratt, *et al. Long Range Plan: Dense matter theory for heavy-ion collisions and neutron stars*, arXiv:2211.02224 [nucl-th].
- [3] G. Aarts, J. Aichelin, C. Allton, A. Athenodorou, D. Bachtis, C. Bonanno, N. Brambilla, E. Bratkovskaya, M. Bruno and M. Caselle, *et al. Phase transitions in particle physics - Results and perspectives from lattice Quantum Chromo-Dynamics*, arXiv:2301.04382 [hep-lat].
- [4] M. Arslanodk, S. A. Bass, A. A. Baty, I. Bautista, C. Beattie, F. Becattini, R. Bellwied, Y. Berdnikov, A. Berdnikov and J. Bielcik, *et al. Hot QCD white paper*, arXiv:2303.17254 [nucl-ex].
- [5] P. Achenbach, D. Adhikari, A. Afanasev, F. Afzal, C. A. Aidala, A. Al-bataineh, D. K. Almaalol, M. Amarian, D. Androic and W. R. Armstrong, *et al. The present and future of QCD*, arXiv:2303.02579 [hep-ph].
- [6] K. Zhou, L. Wang, L. G. Pang and S. Shi, *Exploring QCD matter in extreme conditions with machine learning*, arXiv:2303.15136 [hep-ph].
- [7] C. J. Horowitz, J. Piekarewicz and B. Reed, *Insights into nuclear saturation density from parity violating electron scattering*, Phys. Rev. C **102**, 044321 (2020), arXiv:2007.07117 [nucl-th].
- D. Oliinychenko, A. Sorensen, V. Koch and L. McLerran, *Sensitivity of Au+Au collisions to the symmetric nuclear matter equation of state at 2 - 5 nuclear saturation densities*, arXiv:2208.11996 [nucl-th].
- [8] J. Wambach, *Baryon-rich QCD matter*, arXiv:2304.14833 [hep-ph].
- [9] K. Yagi, T. Hatsuda and Y. Miake, *Quark-gluon plasma: From big bang to little bang*, Camb. Monogr. Part. Phys. Nucl. Phys. Cosmol. **23**, Cambridge University Press, 2005.
- [10] M. G. Alford, A. Schmitt, K. Rajagopal and T. Schäfer, *Color superconductivity in dense quark matter*, Rev. Mod. Phys. **80**, 1455 (2008), arXiv:0709.4635 [hep-ph].
- [11] M. G. Alford, K. Rajagopal and F. Wilczek, *Color flavor locking and chiral symmetry breaking in high density QCD*, Nucl. Phys. B **537**, 443 (1999), arXiv:hep-ph/9804403 [hep-ph].
- [12] E. J. Ferrer and V. de la Incera, *Magnetic dual chiral density wave: A candidate quark matter phase for the interior of neutron stars*, Universe **7**, 458 (2021), arXiv:2201.04032 [hep-ph].
- [13] E. J. Ferrer, V. de la Incera and C. Manuel, *Magnetic color flavor locking phase in high density QCD*, Phys. Rev. Lett. **95**, 152002 (2005), arXiv:hep-ph/0503162 [hep-ph].
- L. Paulucci, E. J. Ferrer, V. de la Incera and J. E. Horvath, *Equation of state for the MCFL phase and its implications for compact star models*, Phys. Rev. D **83**, 043009 (2011), arXiv:1010.3041 [astro-ph.HE].
- [14] S. Fayazbakhsh and N. Sadooghi, *Phase diagram of hot magnetized two-flavor color superconducting quark matter*, Phys. Rev. D **83**, 025026 (2011), arXiv:1009.6125 [hep-ph].
- S. Fayazbakhsh and N. Sadooghi, *Color neutral 2SC phase of cold and dense quark matter in the presence of constant magnetic fields*, Phys. Rev. D **82**, 045010 (2010),

- arXiv:1005.5022 [hep-ph].
- [15] D. V. Deryagin, D. Y. Grigoriev and V. A. Rubakov, *Standing wave ground state in high density, zero temperature QCD at large $N(c)$* , Int. J. Mod. Phys. A **7**, 659 (1992).
- [16] E. Shuster and D. T. Son, *On finite density QCD at large $N(c)$* , Nucl. Phys. B **573**, 434 (2000), arXiv:hep-ph/9905448 [hep-ph].
B. Y. Park, M. Rho, A. Wirzba and I. Zahed, *Dense QCD: Overhauser or BCS pairing?*, Phys. Rev. D **62**, 034015 (2000), arXiv:hep-ph/9910347 [hep-ph].
R. Rapp, E. V. Shuryak and I. Zahed, *A chiral crystal in cold QCD matter at intermediate densities?*, Phys. Rev. D **63**, 034008 (2001), arXiv:hep-ph/0008207 [hep-ph].
- [17] E. Nakano and T. Tatsumi, *Chiral symmetry and density wave in quark matter*, Phys. Rev. D **71**, 114006 (2005), arXiv:hep-ph/0411350 [hep-ph].
T. Tatsumi and E. Nakano, *Dual chiral density wave in quark matter*, arXiv:hep-ph/0408294 [hep-ph].
- [18] I. E. Frolov, V. C. Zhukovsky and K. G. Klimenko, *Chiral density waves in quark matter within the Nambu-Jona-Lasinio model in an external magnetic field*, Phys. Rev. D **82**, 076002 (2010), arXiv:1007.2984 [hep-ph].
- [19] E. J. Ferrer and V. de la Incera, *Novel topological effects in dense QCD in a magnetic field*, Nucl. Phys. B **931**, 192 (2018), arXiv:1512.03972 [nucl-th].
- [20] E. J. Ferrer and V. de la Incera, *Dissipationless Hall current in dense quark matter in a magnetic field*, Phys. Lett. B **769**, 208 (2017), arXiv:1611.00660 [nucl-th].
- [21] E. J. Ferrer and V. de la Incera, *Axion-polariton in the magnetic dual chiral density wave phase of dense QCD*, arXiv:2010.02314 [hep-ph].
- [22] W. Gyory and V. de la Incera, *Phase transitions and resilience of the magnetic dual chiral density wave phase at finite temperature and density*, Phys. Rev. D **106**, 016011 (2022), arXiv:2203.14209 [nucl-th].
- [23] L. Rezzolla and O. Zanotti, *Relativistic Hydrodynamics*, Oxford University Press, 2013.
- [24] H. L. Chen, K. Fukushima, X. G. Huang and K. Mameda, *Analogy between rotation and density for Dirac fermions in a magnetic field*, Phys. Rev. D **93**, 104052 (2016), arXiv:1512.08974 [hep-ph].
- [25] N. Sadooghi, S. M. A. Tabatabaee Mehr and F. Taghinafaz, *Inverse magnetorotational catalysis and the phase diagram of a rotating hot and magnetized quark matter*, Phys. Rev. D **104**, 116022 (2021), arXiv:2108.12760 [hep-ph].
- [26] J. Schaffner-Bielich, *Compact Star Physics*, Cambridge University Press, 2020.
- [27] V. E. Ambrus and E. Winstanley, *Rotating quantum states*, Phys. Lett. B **734**, 296 (2014), arXiv:1401.6388 [hep-th].
- [28] V. E. Ambrus and E. Winstanley, *Rotating fermions inside a cylindrical boundary*, Phys. Rev. D **93**, 104014 (2016), arXiv:1512.05239 [hep-th].
- [29] M. N. Chernodub and S. Gongyo, *Interacting fermions in rotation: chiral symmetry restoration, moment of inertia and thermodynamics*, JHEP **01**, 136 (2017), arXiv:1611.02598 [hep-th].
M. N. Chernodub and S. Gongyo, *Effects of rotation and boundaries on chiral symmetry breaking of relativistic fermions*, Phys. Rev. D **95**, 096006 (2017), arXiv:1702.08266 [hep-th].
- [30] M. N. Chernodub and S. Gongyo, *Edge states and thermodynamics of rotating relativistic fermions under magnetic field*, Phys. Rev. D **96**, 096014 (2017), arXiv:1706.08448 [hep-th].
- [31] I. A. Rather, U. Rahaman, V. Dexheimer, A. A. Usmani and S. K. Patra, *Heavy magnetic neutron stars*, Astrophys. J. **917**, 46 (2021) arXiv:2104.05950 [nucl-ph].
- [32] J. Zhao, J. Chen, X. G. Huang and Y. G. Ma, *Electromagnetic fields in ultra-peripheral relativistic heavy-ion collisions*, arXiv:2211.03968 [nucl-th].
- [33] F. Becattini, I. Karpenko, M. Lisa, I. Upszal and S. Voloshin, *Global hyperon polarization at local thermodynamic equilibrium with vorticity, magnetic field and feed-down*, Phys. Rev. C **95**, 054902 (2017), arXiv:1610.02506 [nucl-th].
- [34] S. M. A. Tabatabaee, *Chiral symmetry breaking and phase diagram of dual chiral density wave in a rotating quark matter*, arXiv:2306.11753 [nucl-th].
- [35] M. N. Chernodub, *Inhomogeneous confining-deconfining phases in rotating plasmas*, Phys. Rev. D **103**, 054027 (2021), arXiv:2012.04924 [hep-ph].
- [36] A. J. Niemi and G. W. Semenoff, *Fermion number fractionization in quantum field theory*, Phys. Rept. **135**, 99 (1986).